

Original Article

Cite this article: Liu Y, Jiang S-H, Bagas L, Chen C-L, Han N, and Wan Y-Y (2020) Petrogenesis and metallogenic potential of the Wulanba granite, southern Great Xing'an Range, NE China: constraints from whole-rock and apatite geochemistry. *Geological Magazine* 157: 411–434. <https://doi.org/10.1017/S0016756819000876>

Received: 9 March 2019

Revised: 23 June 2019

Accepted: 3 July 2019

First published online: 6 November 2019


Keywords:

apatite; ore-related rock; Sr–Nd–Pb–Hf isotopes; geochronology; Wulanba granite; Great Xing'an Range

Author for correspondence:

Si-Hong Jiang and Yun-Yang Wan,
Emails: jiangsihong1@163.com
and wanyunyang@cup.edu.cn

Petrogenesis and metallogenic potential of the Wulanba granite, southern Great Xing'an Range, NE China: constraints from whole-rock and apatite geochemistry

Yuan Liu^{1,2}, Si-Hong Jiang², Leon Bagas^{2,3}, Chun-Liang Chen², Ning Han² and Yun-Yang Wan¹ 

¹State Key Laboratory of Petroleum Resources and Prospecting, China University of Petroleum, Beijing 102249, China; ²MNR Key Laboratory of Metallogeny and Mineral Assessment, Institute of Mineral Resources, Chinese Academy of Geological Sciences, Beijing 100037, China and ³Centre for Exploration Targeting, The University of Western Australia, Crawley, WA 6009, Australia

Abstract

The Wulanba granite, consisting of biotite monzogranite and syenogranite, is located in the southern part of the Great Xing'an Range, NE China. Whole-rock major- and trace-element geochemistry suggests the Wulanba granite is a high-K–shoshonitic, slightly peraluminous and highly differentiated I-type granite. The Sr–Nd–Hf isotopes indicate that it originated from partial melting of juvenile crust derived from the depleted mantle with a minor input of old crust. The relatively young T_{2DM} and t_{DM2} ages indicate it was most likely derived from a Late Neoproterozoic to Early Palaeozoic source. We have demonstrated that the biotite monzogranite is the ore-related intrusion of the Haobugao Zn–Fe mineralization based on the following geological, geochronological and geochemical evidence: (1) the chalcopyrite/pyrite in the biotite monzogranite and the continuous mineralization of drill core ZK2508; (2) the consistence of the emplacement age of the biotite monzogranite (~141–140/138 Ma) with the skarn mineralization age (~142 Ma); and (3) the presence of rich ore-forming elements (Fe–Zn–Cu) in the biotite monzogranite, and the similar Pb compositions of the sulfides from the Haobugao deposit and the biotite monzogranite. Compared to the barren syenogranite, the fertile biotite monzogranite is more oxidized, while the edges of the apatite grains in the biotite monzogranite (~123.45) is much higher than that of the barren syenogranite (~73.98). We conclude that these differences reflect unique geochemical signatures, and the geochemical composition of the apatite can be used to infer the economic potential of granites.

1. Introduction

The Great Xing'an Range (GXR) is located in the eastern part of the Central Asian Orogenic Belt (CAOB) where the Palaeozoic Palaeo-Asian tectonic domain is superimposed on the Mesozoic Western Pacific tectonic domain in the east and the Mongol-Okhotsk Ocean tectonic domain in the northwest. This region is believed to have experienced the world's largest amount of juvenile crust formation during Neoproterozoic to Phanerozoic times (Fig. 1) (Nie *et al.* 2002; Jahn, 2004; Wu *et al.* 2011a,b; Zeng *et al.* 2013; Zhai *et al.* 2013). Three periods of granite magmatism occurred in the GXR: Late Palaeozoic calc-alkaline volcanic rocks and later A-type granites, Triassic to Jurassic highly fractionated I- and A-type granites, and Cretaceous I-type granites followed by A-type granites (Li & Yu, 1993; Wang & Zhao, 1997; Wu *et al.* 2000, 2001, 2002; Sun *et al.* 2001). However, distinguishing between the A-type granites and the highly differentiated I-type granites is difficult (Chappell & White, 2001; King *et al.* 2001). In the southern part of the Great Xing'an Range (SGXR), the skarn-type, hydrothermal vein-type and porphyry-type deposits in the Huanggang–Ulanhot polymetallic metallogenic belt are all related to the Early Cretaceous magmatism (~143–129 Ma), which was caused by magmatic underplating in an extensional tectonic environment at < 145 Ma (Fig. 2a) (Zhang *et al.* 2010a; Jia *et al.* 2011; Jiang *et al.* 2011a, 2012, 2017; Zhou *et al.* 2012; Wang, 2015; Liu *et al.* 2016, 2017). As a typical skarn deposit, the geological characteristics, mineralization and ore-forming processes of the Haobugao Zn–Fe deposit have been studied in detail (Fig. 2b, c; Zhang *et al.* 1994; Sheng & Fu, 1999; Wang *et al.* 2004, 2018; Li *et al.* 2016; Liu *et al.* 2017). Liu *et al.* (2018) proposed that the Haobugao skarn-type mineralization (134–139 Ma) is mainly related to the Wulanba granite (137–144 Ma). However, several periods of magmatism have been identified around the mining area (Fig. 2b) (Li *et al.* 2016, 2017). Therefore, apart from geochronological data, direct geological field evidence is required to assess the potential of using magma mineralogy to

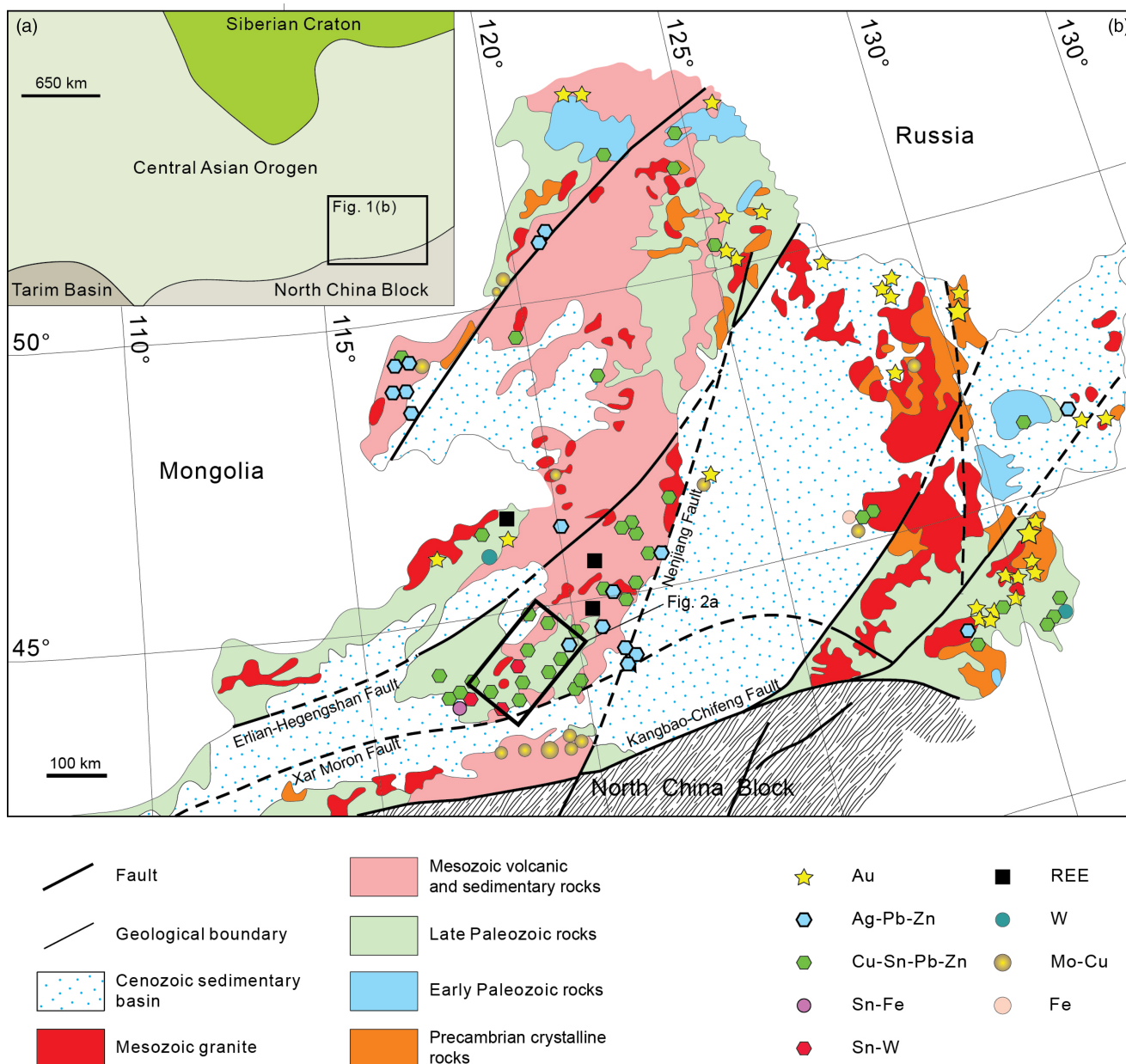


Fig. 1. (Colour online) (a) Simplified geological map showing the location of the Central Asian Orogenic Belt; and (b) geological map of the Great Xing'an Range and its adjacent areas (modified after Liu *et al.* 2017).

identify ore-related rocks. In addition, Liu *et al.* (2018) classified the Wulanba granite as an A-type granite, whereas we classify it as a highly differentiated I-type granite.

Apatite (Ca₅(PO₄)₃(F, OH, Cl)) can record important petrogenetic and metallogenic information concerning the volatile composition and magmatic properties of ore-related rocks (Mathez & Webster, 2005; Marks *et al.* 2012; Scott *et al.* 2015; Pan *et al.* 2016; Chakhmouradian *et al.* 2017; Mitchell *et al.* 2017). In addition, the geochemical composition of apatite may be an effective indicator of potential minerals in porphyry deposits, which could aid in exploration efforts (Ballard *et al.* 2002; Qiu *et al.* 2013; Zhang *et al.* 2017). Although skarn deposits are similar to porphyry deposits (Mao *et al.* 2006; Sillitoe, 2010), the analysis of apatite in skarn deposits is rare (Ding *et al.* 2015;

Zhong *et al.* 2018). Defining the distinct geochemical signatures of the fertile and barren rocks in the Haobugao skarn deposit may enhance our understanding of the role that magmas played in the formation of the deposit. In this study, the major/trace-element geochemistry and the Sr–Nd isotopic compositions of apatite grains from the Wulanba granite were analysed using electron microprobe analysis (EMPA) and laser-ablation inductively coupled plasma mass spectrometry (LA-ICP-MS). Whole-rock geochemical, geochronological and Sr–Nd–Pb–Hf isotopic data were also obtained. In this paper, we attempt to (1) constrain the origin and petrogenesis of the Wulanba granite; (2) identify the ore-related rock; and (3) examine the different geochemical characteristics of the fertile and barren rocks in the Haobugao deposit based on apatite geochemistry.

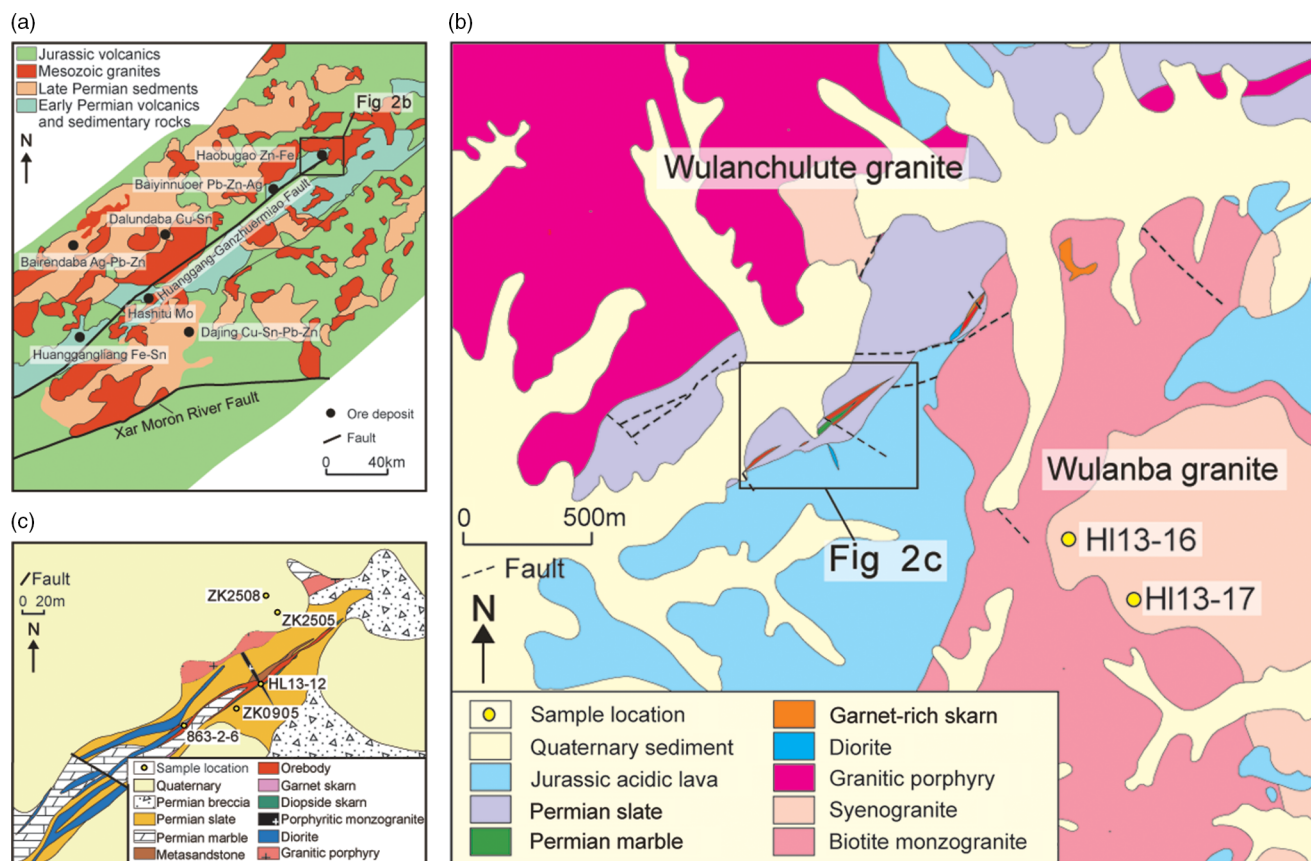


Fig. 2. (Colour online) Geological map of (a) the Huanggangliang–Ganzhu’ermiao metallogenic belt in the southern part of the Great Xing’an Range; (b) the Wulanba granite and its adjacent areas; and (c) the Haobugao Zn–Fe deposit (modified after Liu *et al.* 2017).

2. Regional geology

The GXR is located in the eastern CAOB between the Siberian Craton to the north and the North China Craton to the south (Fig. 1a). The SGXR is bounded by the Erlian–Hegenshan Fault to the north, by the Xar Moron Fault to the south and by the Nenjiang Fault to the northeast (Fig. 1b). This region has a complex geological history characterized by the evolution of the Palaeo-Asian Ocean in Palaeozoic to Early–Middle Triassic times, the closure of the Mongol–Okhotsk Ocean in the northwest and the subduction of the Palaeo-Pacific oceanic plate in the east since Late Triassic time (Wang *et al.* 2006; Li *et al.* 2007; Windley *et al.* 2007; Xu *et al.* 2013). The NE-trending SGXR tectonic domain is characterized by widespread faulting and magmatism. This includes the Huanggang–Ganzhu’ermiao Fault, which hosts Late Mesozoic magmatism and related polymetallic deposits (Fig. 2a) (Zhao & Zhang, 1997; Sheng & Fu, 1999; Ouyang *et al.* 2015). The widespread Mesozoic granites include granodiorites, monzogranites, peralkaline granites and syenogranites, which can be separated into Jurassic and Cretaceous groups (Meng, 2003; Xiao *et al.* 2004; Xu *et al.* 2012). The Yanshanian magmatism changed from felsic to alkaline, and the degree of differentiation of the rocks increased from the early stage of magmatism to the late stage. Spatially, the southwestern part of the SGXR contains felsic intrusive rocks, while the northeastern part contains intermediate-felsic intrusive rocks. The Yanshanian magmatic activity is closely related to the formation of the Cu, Ag, Pb, Zn, W, Mo and Sn deposits (Zhang *et al.* 2011).

The study area contains outcrops of Precambrian orthogneiss and paragneiss unconformably overlain by metamorphosed Palaeozoic volcanic and sedimentary rocks and Jurassic to Cretaceous intermediate to felsic volcanic rocks and sedimentary rocks (Fig. 2a; Rui *et al.* 1994; Zhou *et al.* 2012; Zhai *et al.* 2014b). The Palaeozoic units in the region consist of the felsic volcanic rocks of the Middle Ordovician Duobaoshan Formation and the Early Permian Dashizhai Formation and the Upper Permian sedimentary rocks of the Linxi Formation. The Dashizhai Formation is a shallow submarine volcanic succession, which is composed of felsic and intermediate-mafic rocks in the Huanggang–Ganzhu’ermiao–Wulanhaote area.

The LA-ICP-MS U–Pb zircon ages of the volcanic rocks are similar to those of the plutonic rocks in the region (Ouyang *et al.* 2014). Zhang *et al.* (2010a) proposed that the mafic to intermediate volcanic rocks (174–124 Ma) were derived from the continental lithospheric mantle and formed in an extensional intraplate setting based on their slightly enriched Sr and weakly depleted to slightly enriched Nd isotopic ratios. In contrast, the felsic volcanic rocks have been interpreted to have a mixed mantle and crustal magmatic source based on their wide variations in Ba and Sr and highly positive $\epsilon\text{Nd}(t)$ and $\epsilon\text{Hf}(t)$ values (Zhang *et al.* 2010a).

3. Wulanba granite

Two plutonic rock outcrops occur near the Haobugao Zn–Fe deposit: the ~25 km² Wulanba granite and the ~30 km²

Wulanchulute granite. These granites intrude the Permian and Jurassic strata (Fig. 2b). The Wulanba granite, which consists of biotite monzogranites and syenogranites, was emplaced at 137–144 Ma, while the Wulanchulute granite, which is a granitic porphyry, was emplaced at 140–142 Ma (Li *et al.* 2016). The Haobugao Zn–Fe mineralization principally occurs in the skarn zones, which formed in the contact zone between the Wulanba granite and marine pyroclastic rocks and marble of the Lower Permian Dashizhai Formation (Fig. 2b, c) (Sheng & Fu, 1999; Liu *et al.* 2017). The biotite monzogranite of the Wulanba granite is pale red (Fig. 3a) and consists of perthitic K-feldspar (35–50 vol. %; 1.0–2.5 mm) with carlsbad twinning, plagioclase (20–30 vol. %, 0.2–2.0 mm) with polysynthetic twinning, quartz (15–35 vol. %; 0.5–2.0 mm), biotite (5–15 vol. %; 0.25–1.0 mm) with dark-brown pleochroism, and accessory magnetite, apatite, titanite and zircon (Fig. 3c). Based on photographs, the samples are also locally hydrothermally altered, including the partial alteration of K-feldspar to sericite, variable alteration of biotite to sericite-chlorite, and alteration of plagioclase to sericite (Fig. 3b, d). In drill core, the contact between the granite and the carbonate is difficult to pinpoint since it presents as a transitional zone containing chalcopyrite and pyrite (Fig. 3e, g). The medium- to coarse-grained syenogranite is rust brown, equigranular (Fig. 3f) and consists of K-feldspar (65–75 vol. %; 1.0–3.0 mm) with a perthitic texture and weak sericite alteration, plagioclase (5–10 vol. %; 1.0–5.0 mm) with polysynthetic twinning and slight sericitic alteration, quartz (20–30 vol. %; 0.5–1.0 mm), partially chloritized biotite (2–5 vol. %; 0.3 mm) (Fig. 3h), and accessory magnetite and apatite. Significant hydrothermal alteration and mineralization was also observed in the country rock, which mainly consists of slate. Several porphyritic monzogranite, diorite, monzonite porphyry and syenite porphyry dykes were observed in the Haobugao deposit area. These dykes often cut the skarns and orebodies.

4. Samples and analytical methods

We collected biotite monzogranite samples from drill cores ZK2505 and ZK2508, syenogranite from the outcrops, dykes (porphyritic monzogranite and diorite) from tunnels, and sulfides from the drill cores and tunnels. The sample locations are shown in Figure 2b, c and are listed in online Supplementary Material Table S1.

4.a. LA-MC-ICP-MS zircon and apatite U–Pb dating

Six samples were collected from drill cores, outcrops and tunnels for laser-ablation multi-collector inductively coupled plasma mass spectrometry (LA-MC-ICP-MS) U–Pb zircon dating. The samples were crushed and sieved, and the heavy mineral fraction was separated using magnetic and heavy liquid separation methods to concentrate the zircon grains. The zircon grains were then handpicked, mounted in standard GJ-1 epoxy resin mounts and polished. Binocular microscope and cathodoluminescence (CL) images were obtained to study the morphology and internal structures of the zircons. Based on this information, grains were selected for U–Pb isotope analyses. The CL images were taken using a JEOL JXA-8900RL microprobe at the Chinese Academy of Geological Sciences (CAGS) in Beijing. All of the U–Pb isotope data were collected at the Institute of Mineral Resources at CAGS using an LA-MC-ICP-MS and a Thermo-Finnigan Neptune MC-ICP-MS connected to a New Wave 213 Nd–YAG laser-ablation system

(Hou *et al.* 2009). Concordia plots were created and weighted means were calculated using the Isoplot/Ex-V3 Microsoft Excel macro (Ludwig, 2003).

The apatite grains were separated using conventional heavy liquid and magnetic techniques. Then, they were handpicked under a binocular microscope, mounted in epoxy resin and polished down to expose the centres of the grains. CL images of the apatite grains and apatite U–Pb dating analyses of the biotite monzogranite (HL14-46) were obtained using LA-MC-ICP-MS at the Beijing Kehui Testing International Co. Ltd. The operating conditions for the laser-ablation system and the ICP-MS and the data reduction methods are described in detail by Hou *et al.* (2009). Laser sampling was performed using an ESI NWR 193 nm laser-ablation system. An Analytik Jena PQMS Elite ICP-MS was used to acquire ion-signal intensities. The offline raw data selection, integration of the background and analyte signals, time-drift correction and quantitative calibration for the U–Pb dating was performed using ICPMSDataCal. Apatite NW-1 was used as an external standard for the U–Pb dating and was analysed twice for every five to ten analyses. The U, Th and Pb concentrations were calibrated using NIST 610. The concordia diagrams and weighted mean calculations were completed using Isoplot/Ex_ver3.

4.b. Major- and trace-element analyses

The whole-rock geochemical analyses were completed at the Analytical Centre of the Beijing Institute of Geology for Nuclear Industry (ACBIGNI). The major-element compositions were analysed using an X-ray fluorescence spectrometer (Philip PW2404) and the fused disc methods. The trace-element compositions were analysed using an ICP-MS (Finnigan MAT Element I) after acid digestion in Teflon bombs. The analytical precision and accuracy of the analyses were better than 5 % for the major elements and 10 % for the trace elements.

The apatite compositions were determined using EMPA at the Beijing Kehui Testing International Co. Ltd. The EMPA was performed with a fully automated JEOL JXA-8230 electron microprobe equipped with four wavelength dispersive spectrometers with a 15 kV excitation voltage, 10 nA beam current and a 10 µm beam diameter. The peak and background counting times were 20 s for F, S, Cl and Fe and 10 s for Na, Si, P and Ca. Fluorine was always measured in the first cycle because of migration during analysis.

4.c. Sr–Nd and lead isotope analyses

First, the sample powders were spiked with mixed isotopic tracers for the Sr and Nd isotopic analyses, and then they were placed in Savillex Teflon screw-cap beakers and dissolved in distilled HF + HNO₃ at 100 °C for seven days. A conventional cation resin exchange technique was used for element separation. The isotopic analyses were carried out on a Finnigan MAT-262 thermal ionization mass spectrometer (TIMS) at the Beijing Institute of Nuclear Geological Research. The whole-rock Sr–Nd isotopic ratios were determined using an ISOPROBE-T at the ACBIGNI. The ¹⁴⁷Sm/¹⁴⁴Nd and ⁸⁷Rb/⁸⁶Sr ratios were calculated using the Sm, Nd, Rb and Sr concentrations measured using the ICP-MS. The measured ¹⁴³Nd/¹⁴⁴Nd and ⁸⁷Sr/⁸⁶Sr ratios were normalized to ¹⁴⁶Nd/¹⁴⁴Nd = 0.7219 and ⁸⁶Sr/⁸⁸Sr = 0.1194, respectively. The SHINESTU Nd standard and NBS-987 Sr standard were measured during the analyses, yielding a ¹⁴³Nd/¹⁴⁴Nd ratio of 0.512118 ± 3 (2σ) and a ⁸⁷Sr/⁸⁶Sr ratio of 0.710250 ± 7 (2σ).

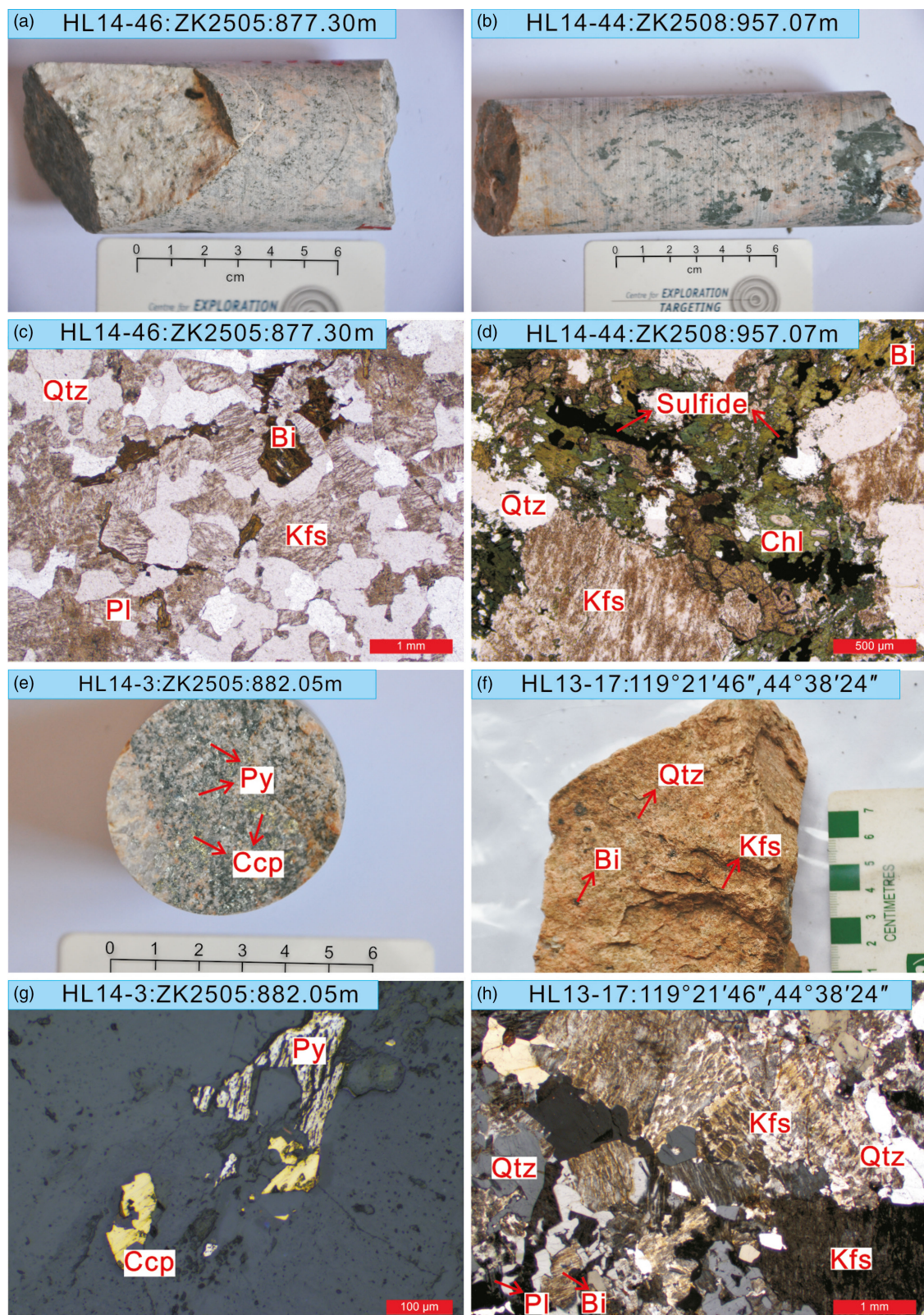


Fig. 3. (Colour online) Photographs and photomicrographs of (a) the biotite monzogranite, 877.30 m, drill core ZK2505 (sample HL14-46); (b) biotite monzogranite with sulfides and chlorite alteration (sample HL14-44); (c) biotite monzogranite containing K-feldspar, plagioclase, quartz and biotite (plane-polarized light); (d) sulfides and chlorite alteration in the biotite monzogranite (plane-polarized light); (e) pyrite and chalcopyrite mineralization in the biotite monzogranite (sample HL14-3); (f) the medium- to coarse-grained syenogranite (sample HL13-17); (g) pyrite and chalcopyrite mineralization in the biotite monzogranite (reflected light); and (h) syenogranite containing K-feldspar, plagioclase, quartz and partly chloritized biotite (cross-polarized light). Abbreviations of minerals: Qtz – quartz; Kfs – K-feldspar; Chl – chlorite; Pl – plagioclase; Bi – biotite; Py – pyrite; Ccp – chalcopyrite.

The *in situ* apatite Sr–Nd isotopic analyses were conducted using an LA-MC-ICP-MS (New Wave 213 nm + Neptune plus) at the Beijing Kehui Testing International Co. Ltd. The isotopic data was obtained in low resolution static mode. During the experiment, the laser energy was ~80 mJ and the energy density ~5.2 J/cm². A beam diameter of 80 µm and a frequency of 10 Hz were used for the laser denudation. Using the single point denudation mode, the denuded substances were extracted from the sample pool with high-purity He as the carrier gas, mixed with high-purity Ar and N₂, and introduced into the mass spectrometer for isotopic analysis. The He flow rate was 0.7–0.9 L/min and the N₂ flow rate was 4–7 ml/min. A 10 s blank was run prior to the laser denudation for Sr isotopic samples. The integration time of the Sr isotopic samples was 20 s and the integration time of the Nd isotopic samples was 30 s. The Sr isotopic data were corrected to ⁸⁵Rb/⁸⁷Rb = 2.593 to exclude the interference of ⁸⁷Rb in the ⁸⁷Sr values. Using the law of exponential fractionation, ⁸⁸Sr/⁸⁶Sr = 8.375209 was used as an internal standard to correct for the fractionation of ⁸⁷Sr/⁸⁶Sr. The Nd isotopic data was calibrated using ¹⁴⁷Sm/¹⁴⁹Sm = 1.0868 for the mass fractionation of Sm. ¹⁴⁴Sm/¹⁴⁹Sm = 0.22332 was used to account for the interference of ¹⁴⁴Sm with ¹⁴⁴Nd.

The sample powders for Pb isotopic analysis were dissolved in HF and HNO₃ in Savillex Teflon screw-cap beakers placed on a hotplate for seven days at 100 °C. The Pb was separated and purified using the anion resin exchange technique with HBr as the eluant. The isotopic ratios were obtained using the Finnigan MAT-262 TIMS at the Beijing Institute of Nuclear Geological Research. Repeated analysis of standard NBS 981 yielded ²⁰⁴Pb/²⁰⁶Pb = 0.05897 ± 15, ²⁰⁷Pb/²⁰⁶Pb = 0.91445 ± 80 and ²⁰⁸Pb/²⁰⁶Pb = 2.16170 ± 180.

4.d. *In situ* zircon Hf isotopic analysis

In situ zircon Hf isotopic analysis was conducted using a Neptune MC-ICP-MS at the MLR Key Laboratory of Metallogeny and Mineral Assessment at the Institute of Mineral Resources, CAGS. The ICP-MS was connected to a New Wave UP213 UV laser-ablation system with He as the carrier gas and an erosion diameter of 55 L/m. The Hf isotopic analysis and U–Pb dating were conducted on the laser-ablation points (cf. Hou *et al.* 2007). The weighted average value of ¹⁷⁶Hf/¹⁷⁷Hf for zircon international standard GJ1 was 0.282024 ± 0.000023 (2σ, n = 18), which is consistent with and within the error range of reported values (Elhlou *et al.* 2006; Hou *et al.* 2007).

5. Results

5.a. *In situ* U–Pb zircon and apatite geochronology

5.a.1. U–Pb zircon dating

The analysed spots and geochronological data for six samples are presented in online Supplementary Material Table S2. Figure 4 presents the zircon U–Pb concordia diagrams. All of the zircon grains were subhedral to euhedral and exhibited typical oscillatory growth zoning, which is consistent with a magmatic origin.

The Th/U ratios of the zircons from biotite monzogranite samples HL14-45 and HL14-46 were 0.26–0.65 and 0.23–1.11, respectively. Nineteen zircons from sample HL14-45 yielded a weighted mean ²⁰⁶Pb–²³⁸U age of 141 ± 1 Ma (MSWD = 1.2) (Fig. 4a, online Supplementary Material Table S2), and 22 zircons from sample HL14-46 yielded a weighted mean ²⁰⁶Pb–²³⁸U age of 140 ± 1 Ma (MSWD = 0.94) (Fig. 4b, online Supplementary

Material Table S2). Within error, these two ages are the same and are taken to be the crystallization age of the biotite monzogranite.

Two syenogranite samples (HL13-16 and HL13-17) were selected for U–Pb zircon dating. The Th/U ratios of the zircons from samples HL13-16 and HL13-17 were 0.41–0.86 and 0.42–1.30, respectively. Nine zircons from sample HL13-16 yielded a weighted mean ²⁰⁶Pb–²³⁸U age of 142 ± 1 Ma (MSWD = 1.7) (Fig. 4c, online Supplementary Material Table S2), and 14 zircons from sample HL13-17 yielded a weighted mean ²⁰⁶Pb–²³⁸U age of 146 ± 1 Ma (MSWD = 1.3) (Fig. 4d, online Supplementary Material Table S2). These results indicate that the crystallization age of the syenogranite is ~146–142 Ma.

The Th/U ratios of the zircons from the porphyritic monzogranite (sample HL13-12) were 0.37–0.76. Nineteen zircons yielded a weighted mean ²⁰⁶Pb–²³⁸U age of 129 ± 1 Ma (MSWD = 3.1) (Fig. 4e, online Supplementary Material Table S2), which was taken to be the crystallization age of the porphyritic monzogranite.

The Th/U ratios of the zircons from the diorite (sample HL863-2-6) were 0.32–0.60. Nineteen zircons yielded a weighted mean ²⁰⁶Pb–²³⁸U age of 135 ± 1 Ma (MSWD = 0.6) (Fig. 4f, online Supplementary Material Table S2), which was taken to be the crystallization age for the diorite.

5.a.2. U–Pb apatite dating

The apatite grains from the biotite monzogranite (sample HL14-46) were dated using the U–Pb method. The separated apatite grains were colourless and predominantly long, prismatic, euhedral crystals or fragments of euhedral crystals (0.02–0.20 mm). Some of the CL images showed obvious zoning (Fig. 6). The LA-ICP-MS U–Pb analytical data for the apatites are presented in online Supplementary Material Table S3, and the concordia and weighted average ²⁰⁷Pb corrected age plots are shown in Figure 4g. All of the U–Pb ages were calculated at a 95 % confidence level. These apatite grains yielded a weighted average ²⁰⁷Pb-corrected age of 138.2 ± 7.3 Ma (MSWD = 3.1, n = 17). Within error, this is the same age as that determined from the zircons and is taken to be the crystallization age of the biotite monzogranite.

5.b. Major- and trace-element compositions

5.b.1. Whole-rock major- and trace-element compositions

The major- and trace-element compositions of seven whole-rock samples are presented in Table 1. The results were normalized to 100 % after accounting for loss on ignition (LOI). The biotite monzogranite and the syenogranite had similar geochemical compositions (Table 1). They are characterized by high SiO₂ contents (71.37–75.47 wt %), low Al₂O₃ contents (11.55–14.89 wt %) and significantly lower MgO contents (0.03–0.67 wt %). Their Na₂O contents ranged from 2.92 to 3.95 wt %, and their K₂O contents ranged from 4.46 to 6.15 wt %. The SiO₂ content of sample HL14-45 (67.36 wt %) was lower than those of the other Wulanba granite samples, but it had higher Al₂O₃ (14.89 wt %), MgO (0.67 wt %), Na₂O (3.95 wt %) and K₂O (5.81 wt %) contents, indicating that it may have been slightly hydrothermally altered. These granite samples are slightly peraluminous high-K–shoshonites with A/CNK values of 0.87–1.06 (<1.1). The chemical index of alteration (CIA = (Al₂O₃/(Al₂O₃ + CaO* + Na₂O + K₂O))*100) estimates the extent of weathering and alteration (Nesbitt & Young, 1982). Fresh basalt has a CIA value of 30–45, whereas fresh monzogranite and granodiorite have higher values ranging from

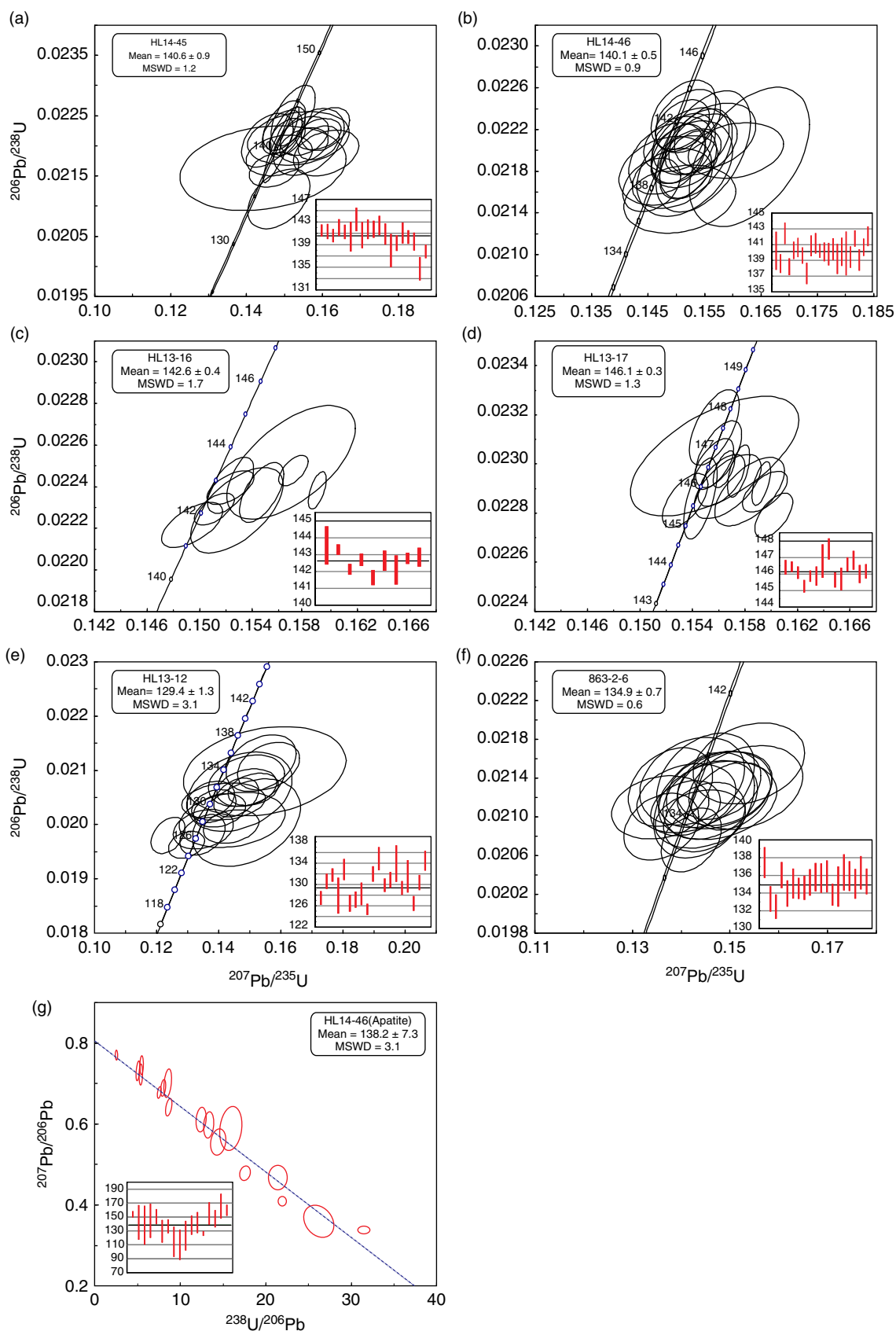


Fig. 4. (Colour online) (a–f) Zircon and (g) apatite U–Pb concordia diagrams.

Table 1. Major- and trace-element compositions of the Wulanba granite

Lithology	Biotite monzogranite					Syenogranite	
	Sample No.	HL14-2	HL14-3	HL14-44	HL14-45	HL14-46	HL13-16
SiO ₂	73.98	74.98	71.37	67.36	74.77	75.47	74.71
TiO ₂	0.25	0.22	0.08	0.45	0.33	0.07	0.07
Al ₂ O ₃	12.86	12.53	11.55	14.89	12.07	13.22	13.33
TFe ₂ O ₃	1.79	1.87	2.13	3.99	2.55	0.82	0.92
MnO	0.02	0.04	0.25	0.08	0.06	0.01	0.01
MgO	0.34	0.35	0.28	0.67	0.49	0.07	0.03
CaO	0.61	0.90	1.39	1.47	0.96	0.37	0.58
Na ₂ O	2.92	3.60	3.10	3.95	3.13	3.85	3.89
K ₂ O	6.15	4.46	5.24	5.81	4.61	5.06	5.29
P ₂ O ₅	0.07	0.04	0.02	0.11	0.08	0.01	0.01
LOI	0.91	0.93	0.27	1.19	0.84	0.72	0.84
Total	99.72	99.74	99.47	99.62	99.64	99.67	99.68
DI	93.55	92.09	86.83	86.79	90.47	96.20	95.70
A/CNK	1.02	1.01	0.87	0.96	1.02	1.06	1.01
A/NK	1.12	1.17	1.07	1.16	1.19	1.12	1.10
AR	2.53	3.31	2.84	2.87	2.85	3.61	3.54
σ ₄₃	2.64	2.02	2.44	3.87	1.88	2.44	2.65
Na ₂ O + K ₂ O	9.07	8.06	8.34	9.76	7.74	8.91	9.18
Na ₂ O/K ₂ O	0.47	0.81	0.59	0.68	0.68	0.76	0.74
(Na ₂ O + K ₂ O)CaO	7.79	9.01	6.00	6.64	8.04	24.08	15.83
CIA	57.06	58.32	54.28	57.01	58.10	58.76	57.73
La	19.9	29.90	27.60	48.40	60.00	15.57	13.29
Ce	36	70.60	82.80	107.00	116.00	43.30	41.08
Pr	4.79	9.41	14.60	14.00	14.00	4.35	4.28
Nd	18.9	37.30	70.80	51.10	46.60	16.02	17.58
Sm	4.57	8.51	22.40	10.60	7.42	3.85	4.60
Eu	0.427	0.16	0.14	0.29	0.45	0.23	0.13
Gd	3.54	8.09	21.60	8.28	6.52	3.70	4.91
Tb	0.727	1.63	4.07	1.45	1.07	0.71	1.03
Dy	4.27	10.30	25.30	10.60	5.58	5.08	7.64
Ho	0.759	2.13	4.71	2.06	1.12	1.05	1.66
Er	2.45	6.58	14.50	7.46	3.31	3.36	5.26
Tm	0.40	1.28	2.51	1.38	0.61	0.56	0.89
Yb	2.7	8.07	15.80	10.50	3.49	3.74	5.68
Lu	0.405	0.99	2.22	1.37	0.55	0.57	0.87
Y	29.3	62.70	134.00	71.20	38.80	33.07	51.52
REE	99.84	194.95	309.05	274.49	266.72	102.10	108.91
LREE	84.59	155.88	218.34	231.39	244.47	83.34	80.96
HREE	15.25	39.07	90.71	43.10	22.25	18.77	27.95
LREE/HREE	5.55	3.99	2.41	5.37	10.99	4.44	2.90
La _N /Yb _N	5.29	2.66	1.25	3.31	12.33	2.98	1.68
La _N /Sm _N	2.74	2.21	0.78	2.87	5.09	2.54	1.82

(Continued)

Table 1. (Continued)

Lithology	Biotite monzogranite					Syenogranite	
	HL14-2	HL14-3	HL14-44	HL14-45	HL14-46	HL13-16	HL13-17
Sample No.							
δEu	0.31	0.06	0.02	0.09	0.19	0.18	0.09
δCe	0.88	1.02	1.00	0.99	0.95	1.27	1.33
Li	17.3	13.30	5.18	22.80	20.30	10.88	9.50
Be	2.13	6.36	4.18	7.34	3.84	4.34	4.48
Sc	1.85	1.84	3.67	2.89	2.59	1.53	1.35
V	12.7	8.93	3.37	27.10	18.30	2.27	1.16
Cr	5.18	2.41	2.23	3.68	6.67	0.44	0.36
Co	2.3	2.10	3.77	4.10	3.37	0.38	0.36
Ni	1.51	1.12	1.49	2.09	1.91	0.78	0.82
Cu	5.97	31.60	185.00	37.20	12.90	2.63	2.41
Zn	75.4	366.00	122.00	181.00	314.00	37.86	36.38
Ga	19.3	24.10	23.30	29.30	19.70	22.19	25.69
Rb	208	193	174	335	199	281	232
Sr	101	37	30	81	93	38	20
Ba	907	94	85	193	529	238	77
Nb	12.8	36.30	17.90	32.40	15.60	12.21	15.03
Ta	1.05	4.78	2.18	4.75	1.51	1.39	1.63
Zr	199	188	76	365	249	99	115
Hf	7.02	8.72	4.33	18.00	8.74	4.08	6.22
Cs	4.44	4.81	3.78	9.03	5.47	5.42	4.36
Tl	1.51	1.10	0.77	1.99	1.50	2.26	1.41
Pb	26.4	46.40	17.90	36.60	38.60	25.17	27.82
Th	15.9	47.50	39.60	90.80	24.30	18.47	36.99
U	6.96	18.00	11.90	31.70	7.55	2.63	3.99
10000*Ga/Al	2.84	3.63	3.81	3.72	3.08	2.86	2.78
Rb/Sr	2.06	5.22	5.76	4.16	2.14	7.40	11.83
Sr/Ba	0.11	0.39	0.36	0.42	0.18	0.16	0.25
Nb/Ta	12.19	7.59	8.21	6.82	10.33	8.78	9.21
Zr/Y	6.79	3.00	0.56	5.13	6.47	2.99	2.23
T _{Zr} (°C)	811	806	711	851	833	756	763

45 to 55 (Nesbitt & Young, 1982). The CIA values of all of our samples ranged from 54 to 61 (Table 1), indicating that the majority of the samples are only slightly altered. Therefore, alteration has not affected the geochemical data.

The total rare earth element (ΣREE) values ranged from 99.84 ppm to 309.05 ppm, and the chondrite-normalized REE patterns of all of the samples are slightly right-inclined with moderately fractionated light REEs (LREEs) and heavy REEs (HREEs) (Fig. 5a; Table 1) and Eu/Eu* values of 0.02–0.31. The Wulanba granite has LREE/HREE values ranging from 2.41 to 5.55 (except for a value of 10.99 for sample HL14-46), and La_N/Yb_N values ranging from 1.25 to 5.29 (except for a value of 12.33 for sample HL14-46). All of the samples have similar primitive mantle-normalized trace-element patterns with depletions in the high field strength elements (HFSEs), i.e. Ba, Nb, Sr, P and Ti, and

enrichments in the large ion lithophile elements (LILEs), i.e. Rb, K, Th, U, La, Ce and Nd (Fig. 5b; Table 1). The Rb content (174–335 ppm) was higher than the continental crustal value of 32 ppm (Taylor & McLennan, 1985), indicating that these samples are highly differentiated. In addition, the calculated zircon saturation temperatures (T_{Zr}) of the biotite monzogranites and syenogranites ranged from 711 °C to 851 °C and from 756 °C to 763 °C, respectively (Watson & Harrison, 1983).

5.b.2. Major- and trace-element compositions of apatite

The CL images of the apatite revealed oscillatory zoning, indicating that these grains have not experienced significant alteration (Fig. 6). The apatite in the biotite monzogranite and the syenogranite occurred as euhedral–subhedral crystals. Table 2 lists the major-element compositions of the apatite grains from the Wulanba

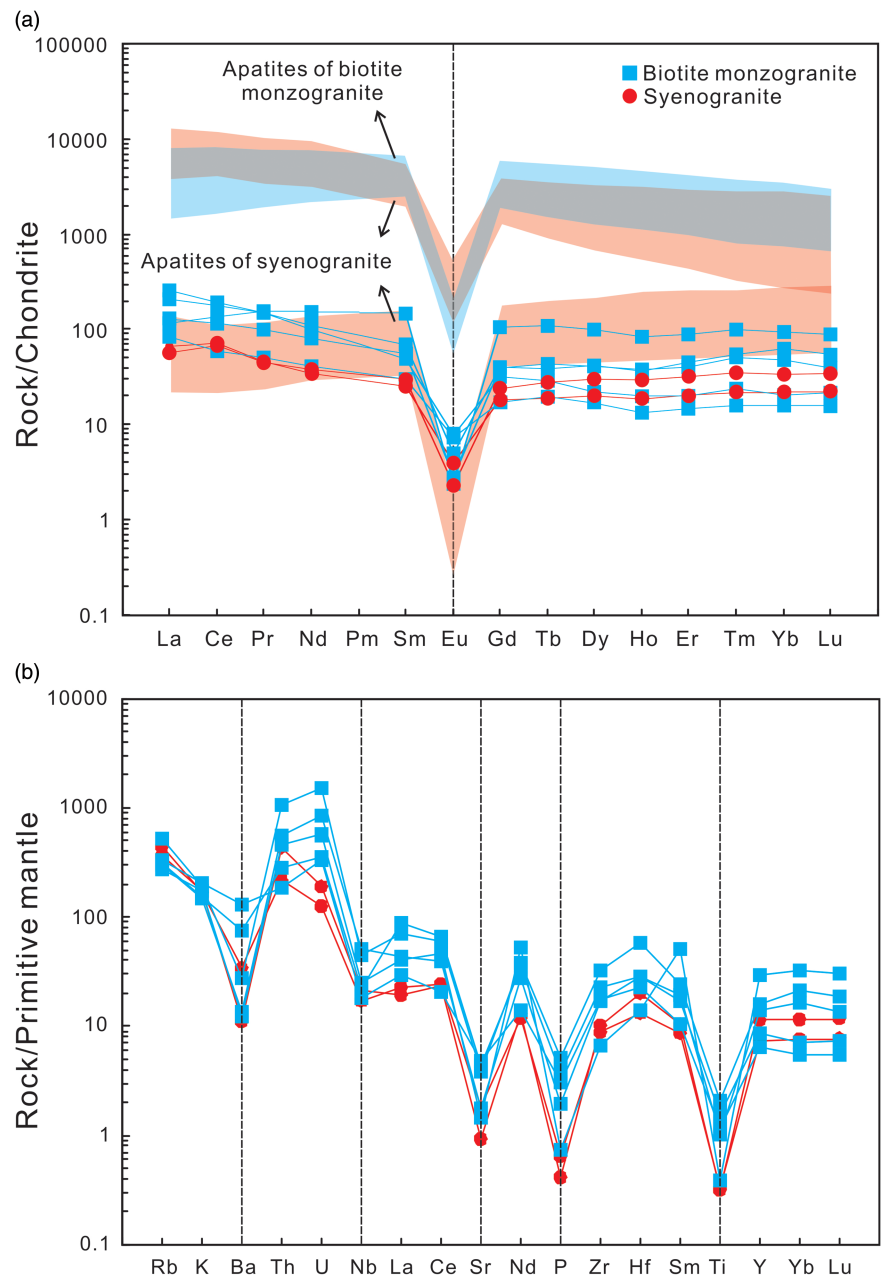


Fig. 5. (Colour online) Trace-element plots for the Wulanba granite and apatite. (a) Chondrite-normalized REE patterns (after Taylor & McLennan, 1985); and (b) primitive mantle-normalized spider diagrams (after Sun & McDonough, 1989).

granite. The P_2O_5 content of the apatite showed little variation with increasing whole-rock SiO_2 content (Fig. 7a), whereas the Na_2O and MnO contents of the apatite from the biotite monzogranite were higher than those of the apatite from the syenogranite (Fig. 7b, c). The apatite samples had CaO contents ranging from 53.24 to 56.06 wt %, FeO contents ranging from 0 to 0.14 wt %, and SO_3 contents ranging from 0 to 0.04 wt %. The Al_2O_3 , MgO , K_2O , TiO_2 , Cr_2O_3 , NiO and chlorine contents were extremely low. However, all of the apatite grains analysed had high fluorine contents (2.79–3.76 wt %; Table 2), classifying them as fluorapatite. On a plot of MnO versus SiO_2 , all of the apatite grains plotted in the magmatic field (Fig. 7d), indicating that the composition of these apatite grains reflects the characteristics of the parent magma.

Online Supplementary Material Table S4 lists the trace-element compositions of the apatite from the Wulanba granite. Similar to the Wulanba granite, the apatite REE patterns exhibit a slight LREE enrichment with LREE/HREE values ranging from 0.65 to 9.68 and distinctly negative Eu anomalies ($\delta Eu = 0.01$ – 0.79) and positive cerium anomalies δCe (0.36–1.69). However, they have significantly higher REE concentrations (2527–17667 ppm) than the Wulanba granite (online Supplementary Material Table S4; Fig. 5a). However, nine apatite grains from sample HL13-16 had ΣREE (34–413 ppm) values similar to those of the granite (Fig. 5a). The relatively low thorium and uranium contents of these nine apatite grains may have been influenced by interaction with later hydrothermal fluids (Fig. 7e). The zirconium and hafnium contents of the apatite from the biotite monzogranite were lower

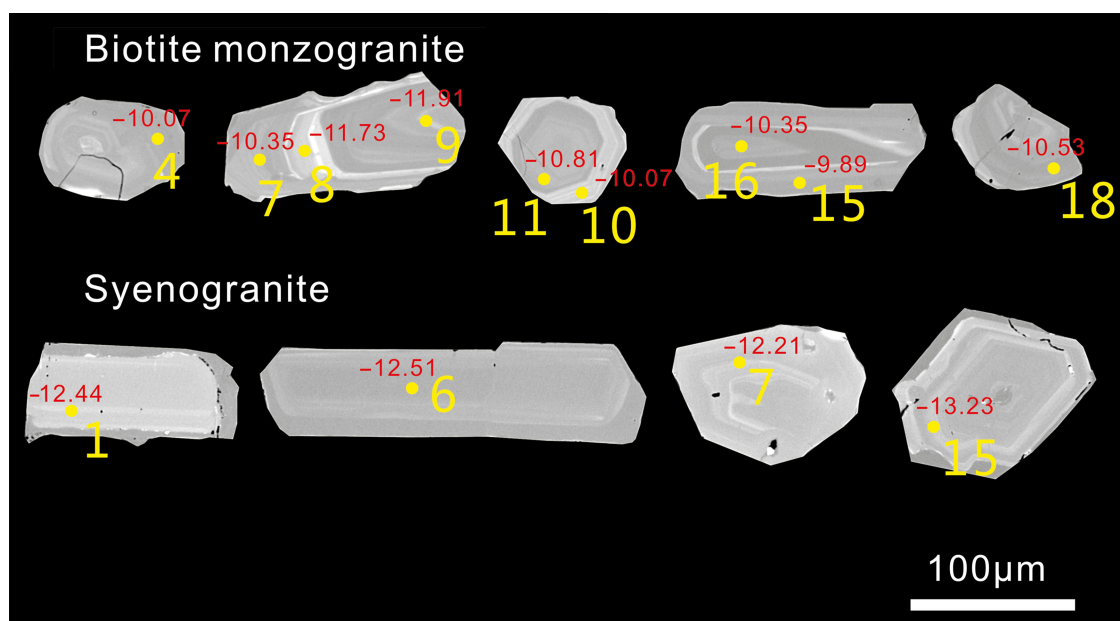


Fig. 6. (Colour online) Cathodoluminescence images of representative apatite grains from the Wulanba granite. Red numbers represent $\log fO_2$ values.

than those of the syenogranite, which also suggests magmatic differentiation (Fig. 7f).

5.c. Sr–Nd–Pb–Hf isotopes

5.c.1. Sr–Nd–Hf isotopes of the whole rock and apatite

The Sr–Nd isotopic compositions of the Wulanba granite and the apatite from it are summarized in online Supplementary Material Table S5. The initial Sr isotope ratios (I_{Sr}) and $\epsilon Nd(t)$ values of the apatite were calculated using the U–Pb apatite age of the biotite monzogranite (138 Ma) and the U–Pb zircon age of the syenogranite (142 Ma). The $^{87}Rb/^{86}Sr$ and $^{87}Sr/^{86}Sr$ ratios of the apatite were very low because of their low Sr contents, so only two usable results were obtained. However, the $^{147}Sm/^{144}Nd$ and $^{143}Nd/^{144}Nd$ ratios obtained were quite good owing to the high Nd contents of the apatite (9–4254 ppm). The calculated I_{Sr} values ranged from 0.70184 to 0.70703 (except for one anomalous value of 0.69888 obtained for sample HL13-17). The $\epsilon Nd(t)$ values ranged from -0.2 to 4.8, and the two-stage depleted mantle Nd model ages (T_{2DM}) ranged from 540 to 950 Ma (online Supplementary Material Table S5).

Four samples were chosen for *in situ* zircon Hf isotopic analysis (online Supplementary Material Table S6). Most of the $^{176}Lu/^{177}Hf$ values of the zircon grains were less than 0.002, indicating little radiogenic Hf accumulation after zircon formation. All of the samples had similar Hf isotopic compositions. The $^{176}Lu/^{177}Hf$ values reflect the Hf isotope compositions of the system during zircon formation (Amelin *et al.* 1999). The $^{176}Hf/^{177}Hf$ ratios of the biotite monzogranite ($t = 141$ Ma for sample HL14-45 and $t = 140$ Ma for sample HL14-46) ranged from 0.282848 to 0.282998, with $\epsilon Hf(t)$ values of 5.6–10.7. The single-stage Hf model ages (T_{DM1}) ranged from 583 to 394 Ma, and the two-stage Hf model ages (t_{DM2}) ranged from 834 to 509 Ma (Fig. 8a, b). The $^{176}Hf/^{177}Hf$ ratios of the syenogranite ranged from 0.282857 to 0.283095 ($t = 142$ Ma for sample HL13-16, and $t = 146$ Ma for sample HL13-17), the $\epsilon Hf(t)$ values from 5.9 to 14.3 (Fig. 8c), the T_{DM1} from 576 to 238 Ma, and the t_{DM2} from 814 to 494 Ma (Fig. 8d).

5.c.2. Lead isotopes

The Wulanba granite and the sulfides from the Haobugao Zn–Fe deposit had relatively similar whole-rock Pb isotope compositions with $(^{206}Pb/^{204}Pb)_i$ values of 18.179–18.739 and 18.026–18.408, $(^{207}Pb/^{204}Pb)_i$ values of 15.509–15.547 and 15.499–15.687, and $(^{208}Pb/^{204}Pb)_i$ values of 38.021–38.119 and 37.986–38.615, respectively (online Supplementary Material Table S7).

6. Discussion

6.a. Petrogenesis

6.a.1. Source of the Wulanba granite

Most Phanerozoic granites in the CAOB are characterized by low initial Sr isotope ratios (<0.707), positive $\epsilon Nd(t)$ values and young Sm–Nd model ages (T_{DM}) of 1200–300 Ma, indicating their ‘juvenile’ character and suggesting derivation from source rocks or magma from the upper mantle (Kovalenko *et al.* 1996; Hong *et al.* 2000; Jahn *et al.* 2000b, 2001; Wu *et al.* 2003; Liu *et al.* 2005, 2007; Shao *et al.* 2010). These characteristics are shared by the Wulanba granite. The syenogranite and the biotite monzogranite were emplaced at 146–142 Ma and 141–140 Ma, respectively, and the cross-cutting diorite and porphyritic monzogranite dykes were emplaced at 134 Ma and 129 Ma, respectively. A high Rb/Sr ratio and low Sr content (<20 ppm) due to fractional crystallization can lead to a significant analytical uncertainty in the initial Sr isotopic composition. This is supported by the low value of 0.69888 for sample HL13-17, which should be >0.7 (Chappell *et al.* 1998; Wu *et al.* 2000; Jahn *et al.* 2001). The other ($^{87}Sr/^{86}Sr$)_i values of the Wulanba granite and the apatite from it vary from 0.70184 to 0.70703. The Wulanba granite and the apatite from it have $\epsilon Nd(t)$ values (-0.2 to 4.8) similar to those of the Early Cretaceous granitic rocks related to the mineralization in the SGXR ($(^{87}Sr/^{86}Sr)_i = 0.70211$ – 0.70945 , $\epsilon Nd(t) = -2.00$ – 2.88), which have a juvenile crustal source (Han *et al.* 1997; Chen *et al.* 2000; Heinhost *et al.* 2000; Wu *et al.* 2000, 2002). Generally, granitic rocks with positive $\epsilon Hf(t)$ values are interpreted to represent partial melting of either the depleted mantle or a

Table 2. EMPA major-element compositions of apatite grains from the Wulanba granite

Sample	P ₂ O ₅	CaO	SiO ₂	Al ₂ O ₃	MnO	MgO	Na ₂ O	K ₂ O	TiO ₂	FeO	Cr ₂ O ₃	NiO	SO ₃	F	Cl	Total	F/Cl	F in magma	Cl in magma	F/Cl in magma	logfO ₂
Apatite from biotite monzogranite																					
HL14-46-01	40.23	55.67	0.27	-	0.09	-	-	-	0.01	0.03	0.03	-	0.03	3.53	-	99.88	-	1.04	-	-	-11.32
HL14-46-02	40.79	55.52	0.22	-	-	-	0.05	-	-	-	0.02	-	-	3.06	-	99.66	-	0.90	-	-	-
HL14-46-03	39.08	55.50	2.44	-	0.10	0.02	0.04	-	-	0.06	-	-	-	3.27	0.00600	100.52	544.50	0.96	0.00750	128.12	-11.52
HL14-46-04	40.78	55.28	0.50	-	0.02	-	-	-	0.07	0.05	-	-	-	3.76	-	100.45	-	1.10	-	-	-10.07
HL14-46-05	40.86	55.09	0.59	-	0.11	0.01	0.02	-	-	0.07	0.02	-	-	3.16	-	99.93	-	0.93	-	-	-11.66
HL14-46-06	40.76	54.76	0.79	-	0.02	-	0.06	-	0.04	0.03	-	-	0.02	2.92	0.00500	99.40	584.60	0.86	0.00625	137.55	-10.14
HL14-46-07	39.64	54.46	0.66	-	0.04	0.01	0.03	-	-	-	-	0.05	-	3.21	0.00700	98.10	457.86	0.94	0.00875	107.73	-10.35
HL14-46-08	39.24	54.62	1.31	-	0.12	0.03	0.04	-	0.07	-	-	-	0.02	2.83	-	98.28	-	0.83	-	-	-11.73
HL14-46-09	41.45	55.73	0.34	-	0.13	0.01	0.05	-	-	0.04	-	-	0.01	3.11	-	100.87	-	0.92	-	-	-11.91
HL14-46-10	40.80	54.90	0.52	-	0.02	0.02	0.09	0.01	0.04	0.09	-	-	-	3.14	-	99.61	-	0.92	-	-	-10.07
HL14-46-11	38.64	55.06	1.44	-	0.06	0.01	0.05	-	-	0.03	-	-	-	3.05	-	98.34	-	0.90	-	-	-10.81
HL14-46-12	40.11	55.20	0.65	0.02	0.11	-	0.11	-	-	0.07	-	-	0.01	2.85	-	99.13	-	0.84	-	-	-11.59
HL14-46-13	39.97	54.50	0.54	0.01	0.08	-	0.09	-	0.04	0.03	-	-	0.01	3.08	0.00600	98.35	513.00	0.91	0.00750	120.71	-11.06
HL14-46-14	41.08	55.12	0.47	-	-	-	0.01	-	0.04	0.05	-	0.03	-	3.03	0.00800	99.84	378.25	0.89	0.01000	89.00	-
HL14-46-15	40.79	55.34	0.38	-	0.01	-	0.01	-	-	-	0.01	-	-	3.19	0.00500	99.72	638.00	0.94	0.00625	150.12	-9.89
HL14-46-16	40.40	55.28	0.29	-	0.04	-	0.06	0.01	-	0.02	-	-	0.01	3.04	0.00500	99.15	608.40	0.89	0.00625	143.15	-10.35
HL14-46-17	41.06	55.48	0.47	-	-	-	0.02	-	-	0.01	-	-	0.03	3.45	-	100.52	-	1.01	-	-	-
HL14-46-18	41.23	56.06	0.28	-	0.05	-	0.01	-	0.12	0.06	-	0.02	-	3.31	0.00700	101.14	472.86	0.97	0.00875	111.26	-10.53
HL14-46-19	39.32	54.68	1.46	-	0.13	-	0.08	-	0.05	0.06	-	-	-	3.48	-	99.27	-	1.02	-	-	-11.98
HL14-46-20	39.74	54.05	1.15	-	0.05	0.01	0.09	-	-	0.06	-	-	-	3.55	-	98.71	-	1.04	-	-	-10.60
Apatite from syenogranite																					
HL13-16-01	40.72	54.95	0.23	-	0.16	-	0.10	0.01	0.04	0.05	-	0.01	0.03	3.01	-	99.28	-	0.89	-	-	-12.44
HL13-16-02	39.37	53.24	0.62	-	0.16	-	0.19	-	0.04	0.03	-	-	-	2.95	0.00700	96.61	422.00	0.87	0.00875	99.29	-12.51
HL13-16-03	39.98	54.21	0.54	-	0.25	-	0.10	-	-	0.07	-	-	0.01	3.13	0.01500	98.30	208.40	0.92	0.01875	49.04	-14.03
HL13-16-04	41.30	55.36	0.15	-	0.11	0.01	0.08	0.01	-	0.03	-	-	-	2.86	-	99.91	-	0.84	-	-	-11.66
HL13-16-05	40.77	54.49	0.13	0.01	0.17	-	0.22	-	-	0.03	-	-	0.01	2.99	0.01000	98.83	298.60	0.88	0.01250	70.26	-12.65
HL13-16-06	41.23	54.31	0.13	-	0.16	-	0.20	0.02	-	0.03	-	-	-	3.22	-	99.30	-	0.95	-	-	-12.51
HL13-16-07	39.91	54.49	0.42	0.01	0.16	0.03	0.07	-	0.08	0.03	-	-	0.01	3.43	0.00900	98.65	381.22	1.01	0.01125	89.70	-12.51
HL13-16-08	40.47	54.90	0.42	0.02	0.10	-	0.10	-	0.05	0.04	-	-	-	2.86	0.00500	98.95	572.40	0.84	0.00625	134.68	-11.39
HL13-16-09	39.90	55.15	0.38	-	0.27	0.03	0.18	-	0.02	0.06	-	-	0.03	2.99	-	99.00	-	0.88	-	-	-14.42
HL13-16-10	40.91	54.55	0.14	-	0.14	-	0.15	0.01	0.01	0.12	0.04	-	0.03	3.21	0.01600	99.33	200.81	0.95	0.02000	47.25	-12.19

(Continued)

Table 2. (Continued)

Sample	P ₂ O ₅	CaO	SiO ₂	Al ₂ O ₃	MnO	MgO	Na ₂ O	K ₂ O	TiO ₂	FeO	Cr ₂ O ₃	NiO	SO ₃	F	Cl	Total	F/Cl	F in magma	Cl in magma	F/Cl in magma	logO ₂
HL13-16-11	40.40	54.53	0.13	0.01	0.11	0.01	0.15	-	-	0.04	0.01	0.01	0.01	2.79	-	98.20	-	0.82	-	-	-11.66
HL13-16-12	40.23	54.71	0.34	0.01	0.07	-	0.08	-	0.05	0.09	0.01	0.03	-	2.97	0.00900	98.58	330.22	0.87	0.01125	77.70	-10.93
HL13-16-13	41.04	54.25	0.32	-	0.24	-	0.12	0.02	0.07	0.12	-	-	-	3.21	0.00900	99.38	356.44	0.94	0.01125	83.87	-13.75
HL13-16-14	40.61	54.62	0.43	-	0.24	-	0.14	0.02	0.01	0.07	-	-	-	2.81	0.01200	98.95	233.83	0.83	0.01500	55.02	-13.82
HL13-16-15	40.34	54.31	0.16	-	0.20	0.02	0.15	-	-	0.08	0.01	-	-	3.14	-	98.42	-	0.92	-	-	-13.23
HL13-16-16	41.22	54.86	0.20	0.01	0.17	0.02	0.08	-	-	0.01	0.01	-	-	3.29	-	99.85	-	0.97	-	-	-12.71
HL13-16-17	41.21	54.64	0.23	-	0.25	0.02	0.16	-	0.01	0.09	-	0.03	-	3.16	-	99.81	-	0.93	-	-	-14.08
HL13-16-18	40.63	54.48	0.29	-	0.15	-	0.12	0.01	-	0.06	-	0.02	0.04	3.00	0.01300	98.82	230.85	0.88	0.01625	54.32	-12.31
HL13-16-19	40.37	55.16	0.16	-	0.19	0.01	0.02	-	0.02	0.14	0.01	-	-	2.87	0.00800	98.95	358.63	0.84	0.01000	84.38	-12.90
HL13-16-20	40.91	55.28	0.18	-	0.20	0.01	0.09	0.02	-	0.05	-	-	-	3.05	0.01700	99.78	179.41	0.90	0.02125	42.21	-13.11

juvenile crustal source derived from the depleted mantle (Zhou *et al.* 2012). On the plot of εHf(t) versus T, all of the samples from the study area with high zircon εHf(t) values of 5.6–14.3 plot between the DM (depleted mantle) and CHUR (chondritic uniform reservoir) fields, similar to the Early Cretaceous granites in the SGXR (−0.80 to 14.20), which have been interpreted to have a juvenile crustal source derived from the depleted mantle (Fig. 9) (Guo *et al.* 2009; J. F. Liu, unpub. Ph.D. thesis, Univ. Jilin, 2009; Zhang *et al.* 2010b; Wu *et al.* 2011b; Zhou *et al.* 2011, 2012; Shu *et al.* 2013b; Ouyang *et al.* 2015). The depleted mantle model age represents the time at which the parental magma was derived from a source that had been separated from the depleted mantle; while the depleted mantle Nd (T_{2DM}) and Hf (t_{DM2}) model ages are used to estimate the ages of their protoliths. The Wulanba granite has young Nd model ages (T_{2DM}) of 950–540 Ma and Hf model (t_{DM2}) ages of 834 and 494 Ma. Most of the Nd model ages (T_{2DM}) overlap with the range of the Hf model ages, indicating that they were derived from the Late Neoproterozoic to Early Palaeozoic juvenile crust (Wu *et al.* 1999; Li *et al.* 2014b). The young T_{2DM} and t_{DM2} ages suggest that the SGXR experienced crustal growth during Neoproterozoic to Early Palaeozoic times (Hong *et al.* 2000; Cai *et al.* 2004).

The large range in εHf(t) values along with the T_{2DM} and t_{DM2} ages suggests that the protolith of the Wulanba granite is complex. The lower εNd(t) values of the Cretaceous igneous rocks in this region are due to the involvement of crustal rocks (Jahn *et al.* 2004). The proportion of mantle material involved in the petrogenesis of the Early Cretaceous igneous rocks was estimated by Jahn *et al.* (2000a) to be 62–92%. According to the method proposed by Wu *et al.* (2002), the proportion of juvenile lower crust involved in the petrogenesis of the Wulanba granite is ~60–80%. We speculate that the source rocks may have originated from partial melting of juvenile crust (~60–80%) derived from the depleted mantle with a minor input of older crust (Cai *et al.* 2004; Shao *et al.* 2010).

6.a.2. Petrogenesis of the Wulanba granite

Intermediate-acid magmas cannot be derived directly from partial melting of the mantle (Green, 1980; Defant & Drummond, 1990; Martin, 1999). Theoretically, granitoids can form from magma mixing, assimilation–fractional crystallization (AFC) or melting of the lower crust (Liu *et al.* 2007). The Wulanba granite did not experience significant magma mixing based on the absence of microgranular mafic enclaves (MMEs) (Poli & Tommasini, 1991; Tepley *et al.* 2000). The presence of oscillatory zoned magmatic zircon grains and the Th/U zircon values (>0.1) (Zhou *et al.* 2010) indicate that the zircon grains were not inherited as a result of contamination by the surrounding host rocks. Lin *et al.* (2004) argued that the source of the low-Sr Mesozoic granites in the GXR was composed of young crustal material that originated in the mantle during Phanerozoic crustal growth. Moreover, the chemical compositions of the Late Mesozoic granitic rocks in the SGXR are similar to those of experimental melts derived from basaltic rocks (Ellis & Thompson, 1986; Sisson *et al.* 2005). Chen & Fu (1992) and Chen *et al.* (2005) summarized the three models for the formation of granitic magmas from partial melting of a thickened lower crust. (1) During the main period of continental orogeny, lower crustal thickening caused by the collision of continental plates and the heat generated by tectonic shearing could induce partial melting of the lower crust. (2) After the main orogenic event, tectonic decompression results in dehydration reactions involving hydrous minerals and induced partial melting of the

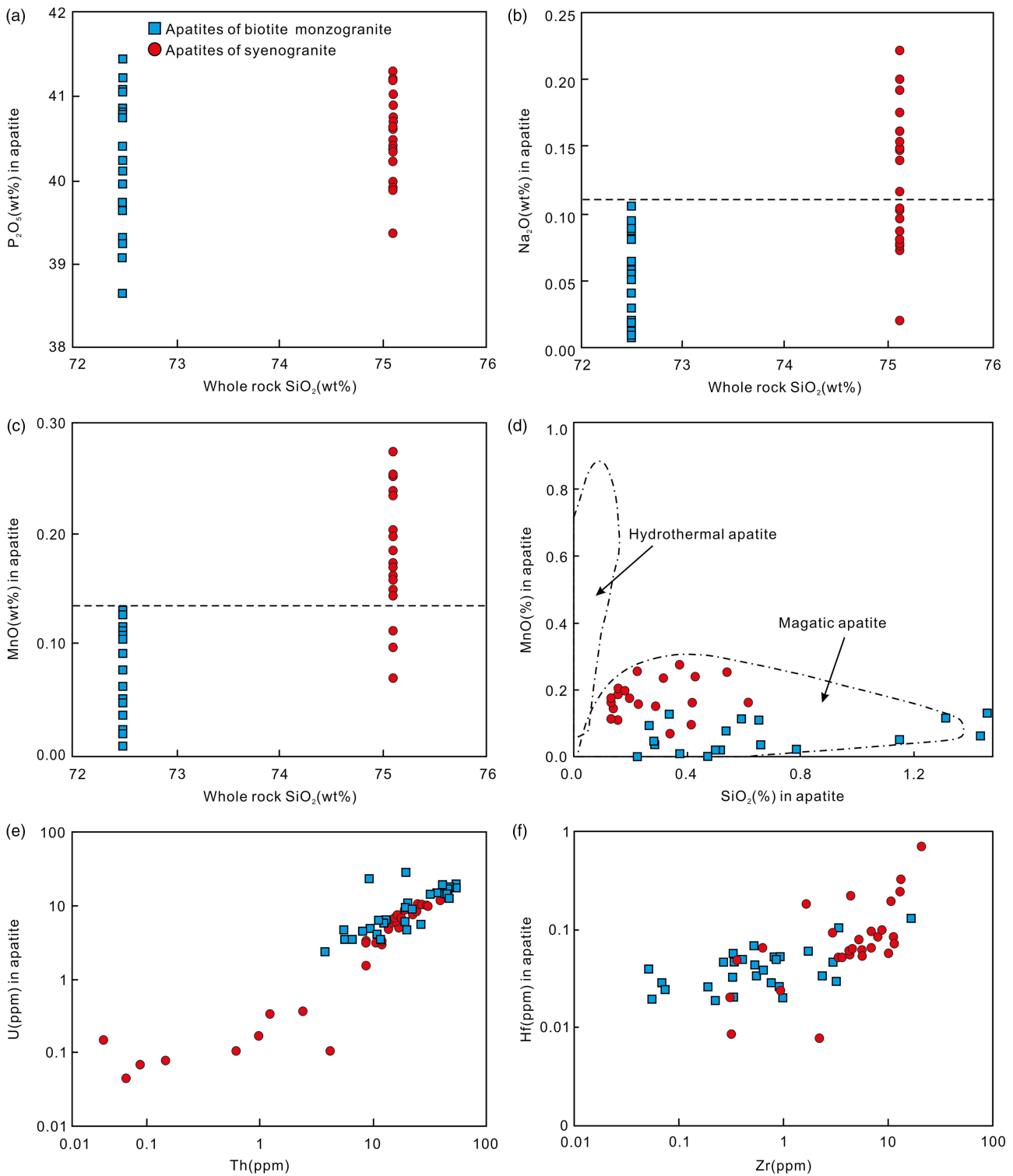


Fig. 7. (Colour online) (a–c) Correlation between the major-element compositions of the apatite and the whole-rock SiO_2 contents; (d) plot of MnO versus SiO_2 , the magmatic and hydrothermal apatite fields are from Chen *et al.* (2017); (e) plot of U versus Th for apatite; and (f) plot of Hf versus Zr for apatite.

crust. (3) After the main orogenic period, lithospheric delamination leads to mantle upwelling and underplating, causing partial melting of the lower crust. The Mesozoic mafic–ultramafic cumulate xenoliths and mafic granulite xenoliths in the GXR have been concluded to be the product of upwelling and asthenospheric underplating (Shao *et al.* 1999, 2001).

Liu *et al.* (2018) classified the Wulanba granite as an A-type granite based on enrichments in Zr, Y and Ga and the plot of Zr versus 1000 Ga/Al . However, it is difficult to distinguish highly differentiated granites from A-type granites. Aluminous A-type granites contain mafic minerals such as annite and/or amphibole, whereas peralkaline A-type granites contain alkali mafic minerals

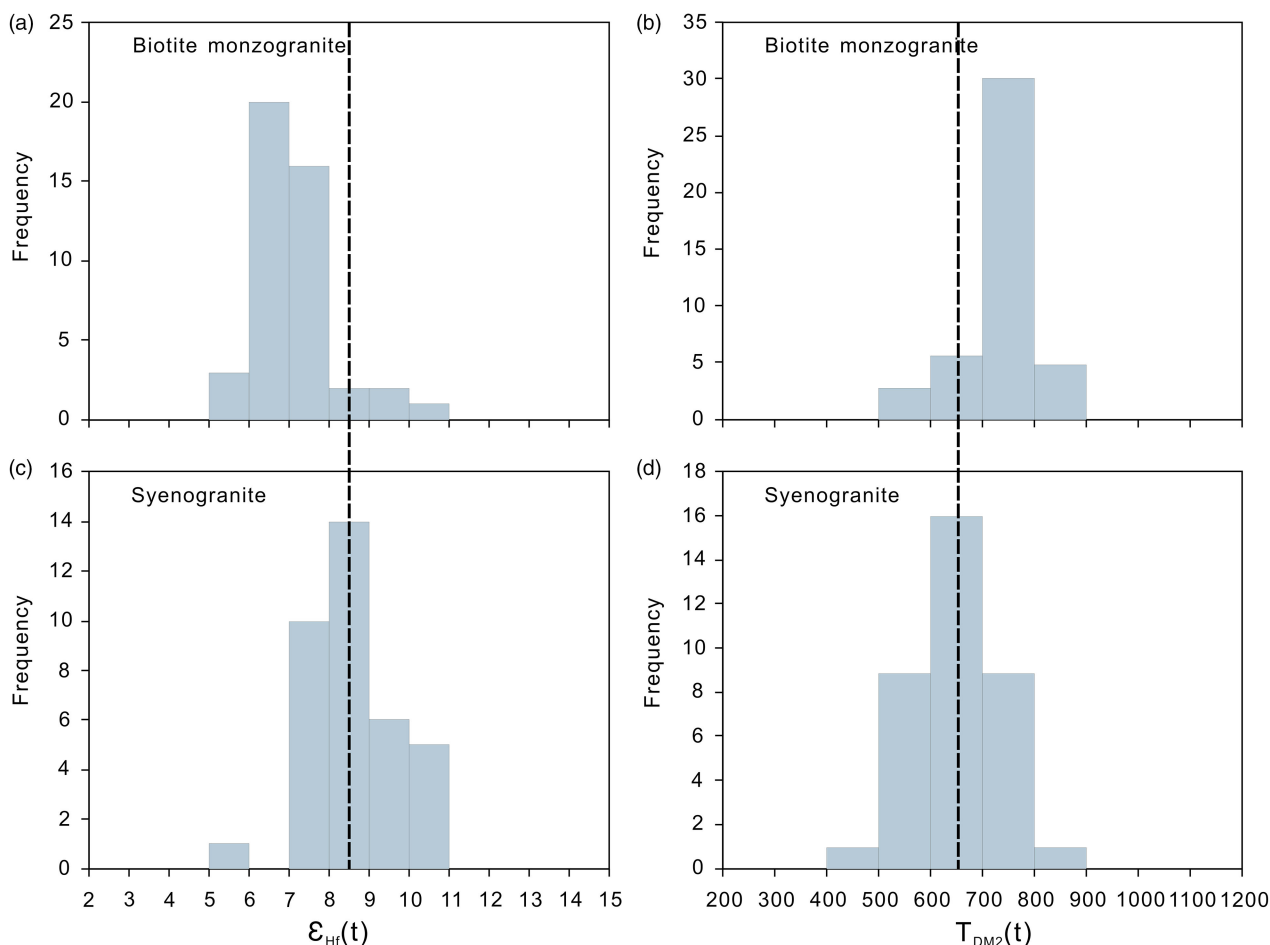


Fig. 8. Histograms of the $\epsilon_{Hf}(t)$ and t_{DM2} values of (a, b) the biotite monzogranite; and (c, d) the syenogranite.

such as arfvedsonite, riebeckite and sodium pyroxene (Wu *et al.* 2002). A-type granites have unique geochemical characteristics, including significant enrichments in alkalis and Ga, Zr, Nb, Y and REEs and high Ga/Al ratios (Whalen *et al.* 1987; Bonin, 2007). However, alkaline Fe–Mg minerals have not been observed in the Wulanba granite. In addition, the geochemical characteristics of the Wulanba granite differ from those of A-type granites. First, the average FeO^T/MgO ratio of the Wulanba granite ranges from 5.28 to 6.98 (except for a value of 27.87 obtained for sample HL14-44 due to its ultra-low MgO content), which is lower than that of A-type granites ($FeO^T/MgO > 10$) (Whalen *et al.* 1987). Second, its average Zr + Ce + Nb + Y content is 335 ppm, which is lower than that of A-type granites (350 ppm). Its average Zr content is 184 ppm (except for a value of 365 ppm obtained for sample HL14-45), which is lower than that of A-type granites (250 ppm). Third, the Ga content is very low (average 23.1 ppm), and the $10^4 \cdot Ga/Al$ ratio varies from 2.84 to 3.81 with an average of 3.42, which is lower than the average value of A-type granites (3.75) suggested by Whalen *et al.* (1987). Most of the samples plot in the highly differentiated granite field (Fig. 10a, b). However, when their FeO^T/MgO ratios are greater than 16, the Zr + Ce + Nb + Y contents and the Ga/Al ratios of differentiated A-type granites can be lower (Bonin, 2007). The low K/Rb and Zr/Hf ratios of these granites indicate magmatic differentiation (Halliday *et al.* 1991; Claiborne *et al.* 2006; Ballouard *et al.* 2016). The Wulanba granite has significant negative Eu anomalies ($\delta Eu = 0.02 - 0.31$), high

K/Ba ratios (56–567), low Zr/Hf ratios (17–29) and Nb/Ta ratios (7–12) (common range for granitic rocks is 15–40 for K/Ba, 35–40 for Zr/Hf and 17–18 for Nb/Ta; Irber, 1999), and depletions in Ba, Sr, P and Ti on the spider diagram, indicating that they are the products of high amounts of differentiation (Miller & Mittlefehldt, 1982, 1984; Jahn *et al.* 2001; Gelman *et al.* 2014). In addition, their high differentiation index (DI) values of 86.79–96.20 are indicative of highly differentiated granites. The Wulanba granite is weakly peraluminous ($A/CNK = 0.87-1.06 < 1.1$) and there is no dolomite, cordierite or garnet in the granite, which is not characteristic of S-type granites with strong peraluminous characteristics. The P_2O_5 content of the Wulanba granite is less than 0.1 wt %, which differs from that of S-type granites (> 0.2 wt %) (Chappell, 1999). In addition, the samples also fall into the I-type granite field on the plot of TiO_2 versus Zr (Fig. 10c). In fact, the Wulanba granite has high SiO_2 and $Na_2O + K_2O$ contents, low Ti, Mn and P contents, and high Rb/Sr and Nb/Ta ratios. In addition, it is significantly enriched in Rb, Th and U and depleted in Ba, Sr and Eu. These characteristics are also consistent with those of highly differentiated I-type granites (Chappell, 1999; Wu *et al.* 2003; Li *et al.* 2007; Zhu *et al.* 2015). Therefore, we conclude that the Wulanba granite is a highly differentiated I-type granite.

The degree of magmatic differentiation of the apatite is exhibited by the $(La/Sm)_N$ and $(Eu/Eu^*)_N$ values. The apatite grains exhibit very slight LREE enrichment. Previous experiments have shown that the apatite/melt partition coefficients of the middle

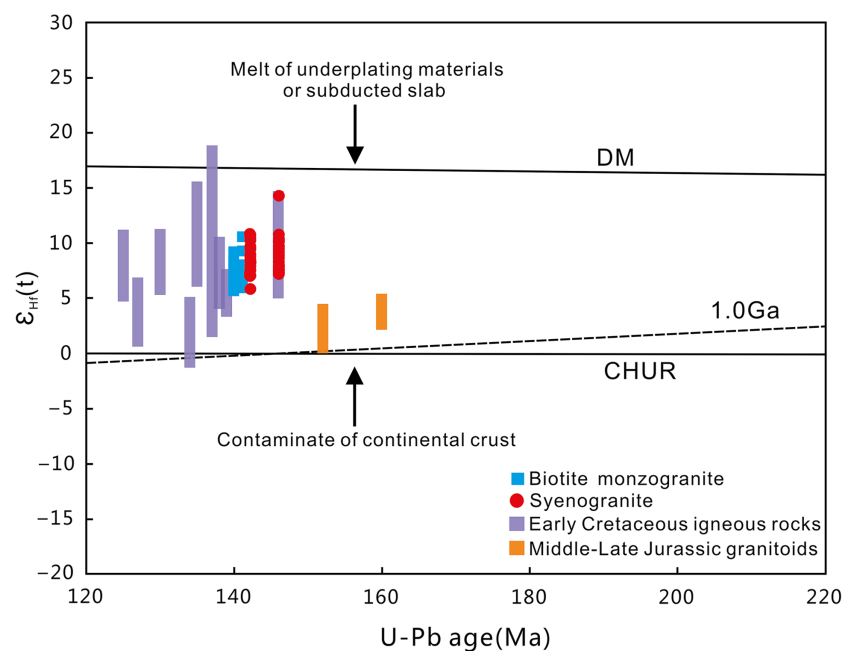


Fig. 9. (Colour online) Initial $\epsilon_{\text{Hf}}(t)$ versus the U–Pb ages of the zircon grains from the Wulanba granite. Data for the Early Cretaceous igneous rocks and Middle to Late Jurassic granites are from Ouyang *et al.* (2015 and references therein). Abbreviations: DM – depleted mantle; CHUR – chondritic uniform reservoir.

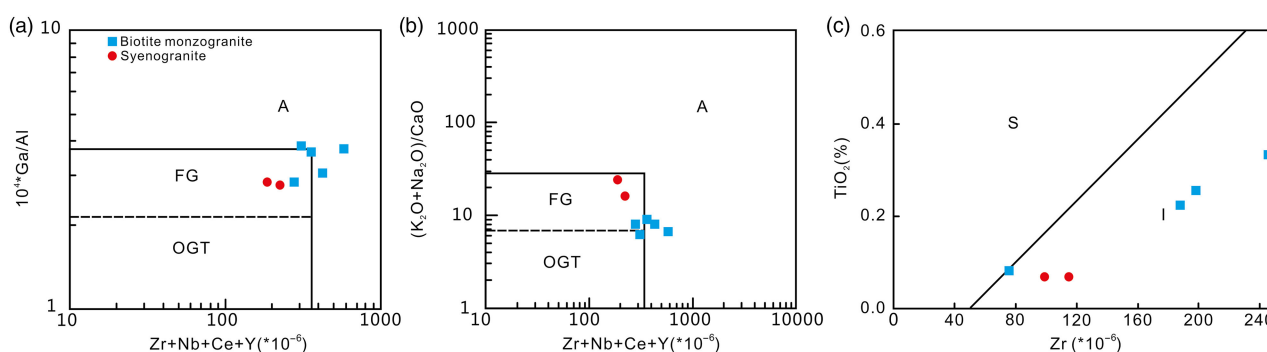


Fig. 10. (Colour online) (a) 10^4Ga/Al versus $(\text{Zr} + \text{Nb} + \text{Ce} + \text{Y})$ discrimination diagram; (b) $(\text{Na}_2\text{O} + \text{K}_2\text{O})/\text{CaO}$ versus $(\text{Zr} + \text{Nb} + \text{Ce} + \text{Y})$ discrimination diagram; and (c) TiO_2 versus Zr discrimination diagram. A – A-type granite; FG – fractionated I-, S- and M-type granites; OGT – unfractionated I-, S- and M-type granites. The base diagrams for figures (a) and (b) are from Whalen *et al.* (1987).

REEs are higher than those of the LREEs and HREEs (Watson & Green, 1981; Fujimaki, 1986), which causes the $(\text{La}/\text{Sm})_{\text{N}}$ values of the apatite grains (0.54–2.81) to be lower than those of the melt (0.78–5.09). Crystallization of plagioclase depletes the Eu value of the magma, resulting in the low Eu content of the apatite, which crystallizes later. Therefore, the significantly negative Eu anomalies of the apatite were most likely caused by the crystallization of plagioclase before the apatite crystallized.

6.b. Constraints on Zn–Fe mineralization

6.b.1. Ore-related rocks

The evolution of northeastern China was controlled by the closure of the Palaeo-Asian Ocean at ~ 250 Ma, which was characterized by crustal accretion and the amalgamation of micro-blocks and terranes in Palaeozoic time and possibly extension until Early–Middle Triassic times (Jahn, 2004; Windley *et al.* 2007; Xiao *et al.* 2009; Jiang *et al.* 2011b; Wu *et al.* 2011b; Han *et al.* 2012; Li *et al.* 2014a,b). In Late Jurassic to Early Cretaceous times,

the subduction of the Palaeo-Pacific Plate and the closure of the Mongol–Okhotsk Ocean caused lithosphere delamination and asthenosphere upwelling (Ouyang *et al.* 2015; Jiang *et al.* 2018). As a result, strong crust–mantle interaction occurred and N–S-striking sinistral shear zones developed, e.g. the NE-striking Huanggang–Ganzhu’ermiao Fault, which played a significant role in controlling the magmatism and mineralization in the SGXR. Therefore, a series of mineralization, granite emplacement, exhumation of metamorphic core complexes and large-scale lithosphere destruction occurred during Early Cretaceous time, indicating an extensional setting (140–120 Ma) (Gao *et al.* 2002; Wu *et al.* 2002, 2005; Mao *et al.* 2005, 2008, 2010; Wang *et al.* 2006; Zhang *et al.* 2010a; Zhu *et al.* 2011; Li *et al.* 2012). As a skarn deposit, the typical lithological succession observed in drill core ZK2508 near the Haobugao deposit (Fig. 11) includes biotite monzogranite, followed by a mineralized garnet skarn, mineralized tuff and mineralized slate from bottom to top. Silicification, chlorinification and carbonation of the various units was also observed. In addition, sulfides such as chalcopyrite and pyrite were observed

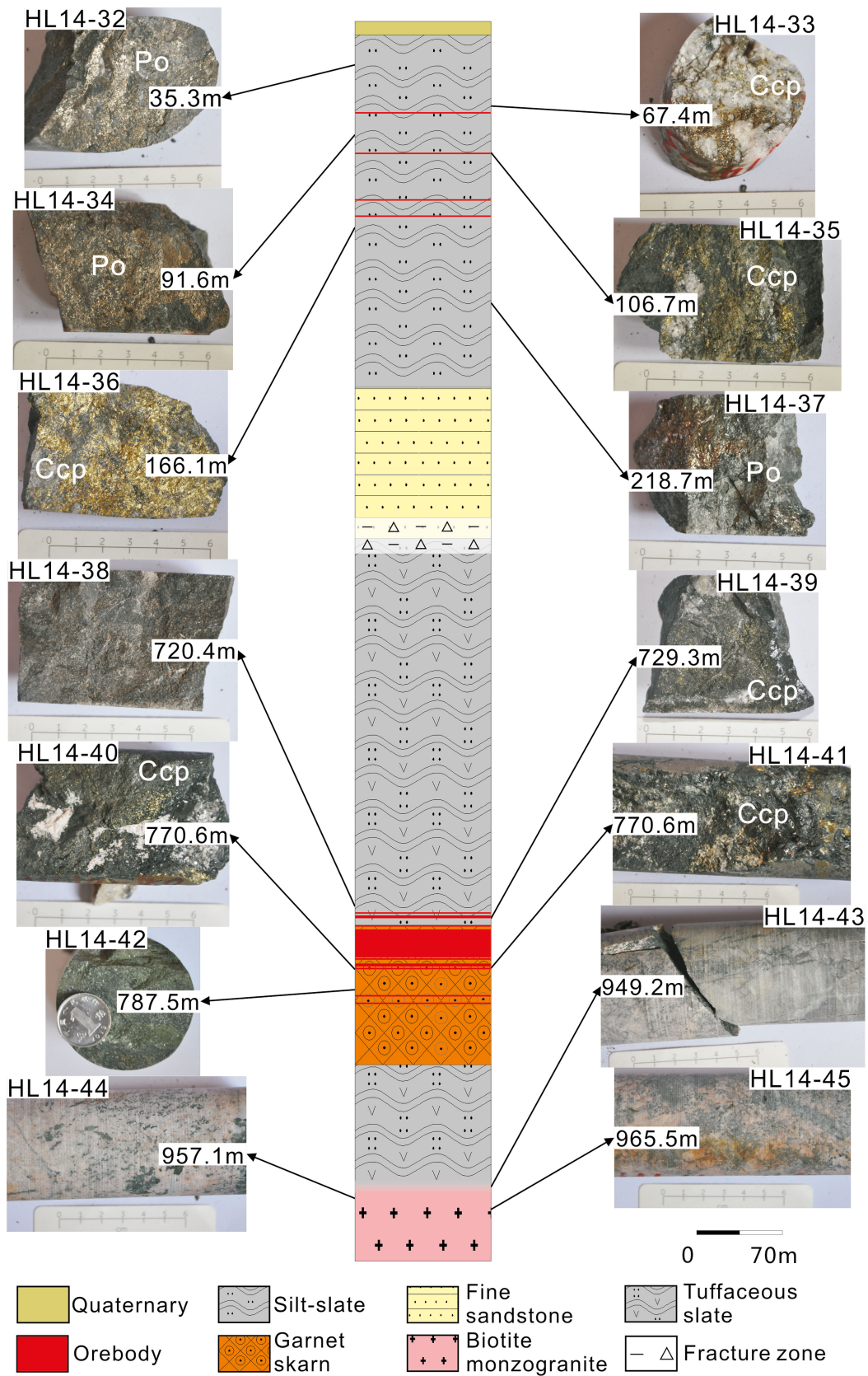


Fig. 11. (Colour online) Samples from drill core ZK2508 (~1000 m) containing biotite monzogranite → mineralized garnet skarn → mineralized tuffaceous slate → mineralized slate from deep to shallow, demonstrating that the biotite granite is the ore-related intrusion.

Fig. 12. (Colour online) Lead isotope compositions of the Wulanba granite and sulfides (base map modified after Ouyang *et al.* 2015). Data for the mantle, orogen, and lower and upper crust evolution curves are from Zartman & Doe (1981), data for the Mesozoic intrusive rocks in the SGXR are from Zhao & Zhang (1997), Chu *et al.* (2001), Xiao *et al.* (2004), Zhu *et al.* (2006), Guo *et al.* (2010) and Jiang *et al.* (2010), and data for the sulfide minerals in the SGXR are from Ouyang *et al.* (2015 and references therein).

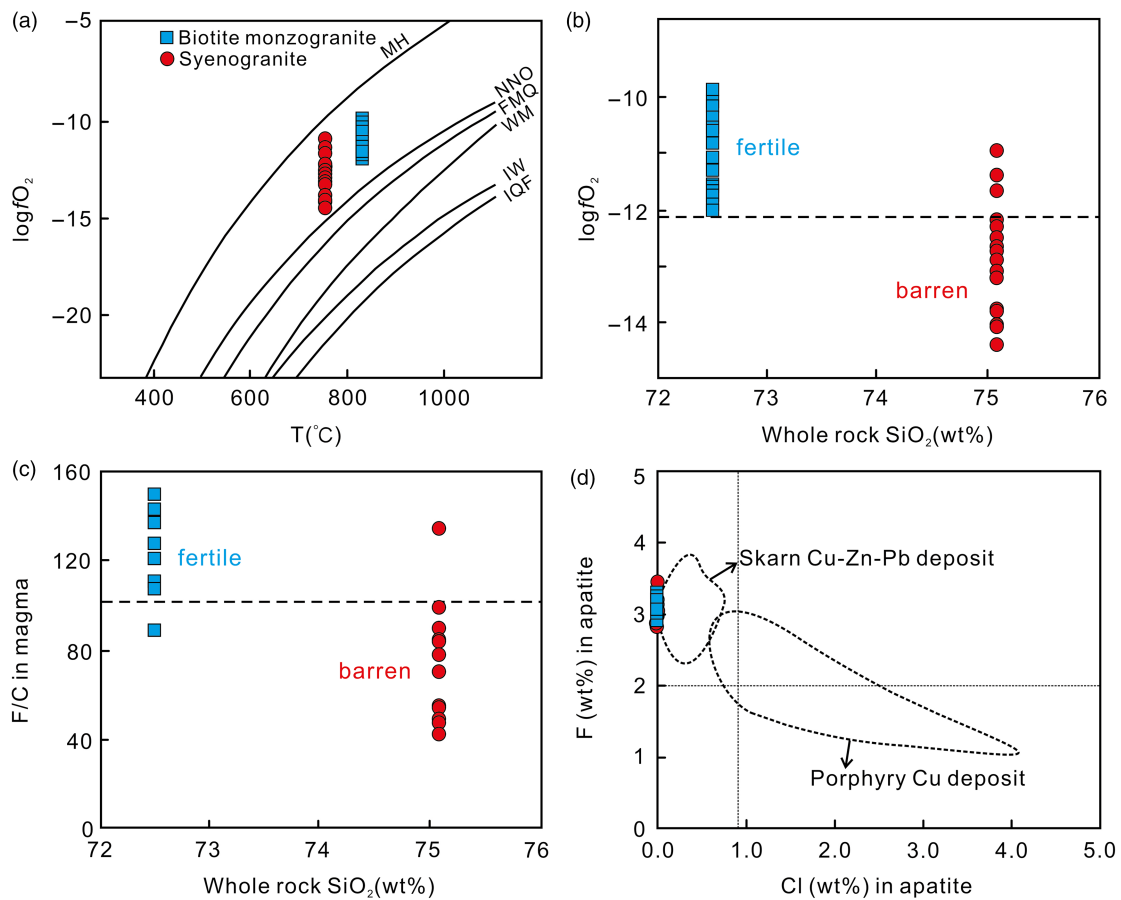
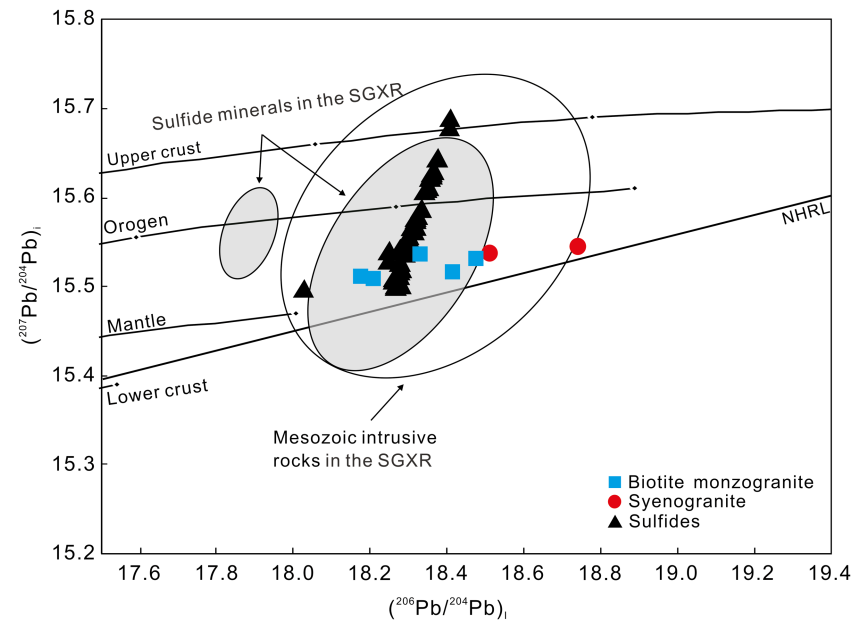


Fig. 13. (Colour online) (a) Plot of $\log fO_2$ versus T ($^{\circ}C$) for the Wulanba granite. In this study, the $\log fO_2$ values were calculated using the method of Miles *et al.* (2014) and the temperature is the T_{Zr} . The oxygen fugacity buffer data are from Eugster & Wones (1962). MH – magnetite–haematite buffer; NNO – NiNiO; FMQ – fayalite–magnetite–quartz buffer; WM – wustite–magnetite; IW – iron–wustite buffer; IQF – iron–quartz–fayalite. (b) Plot of whole-rock SiO_2 (wt %) versus $\log fO_2$; (c) F/Cl of the magma versus whole-rock SiO_2 (wt %); and (d) plot of F (wt %) versus Cl (wt %) for the apatite. The data for the skarn Cu–Zn–Pb deposits and porphyry Cu deposits are from Zhong *et al.* (2018).

in the biotite monzogranite (Fig. 3e, g). These geological characteristics undoubtedly prove that the biotite monzogranite contributed to mineralization. The U–Pb zircon ages of the biotite monzogranite (141–140 Ma) are consistent with the timing of the Haobugao Zn–Fe mineralization (142 Ma) (Liu *et al.* 2017), suggesting a genetic relationship between the Zn–Fe mineralization and the emplacement of the biotite monzogranite. Spatially, along the Huanggang–Ganzhu’ermiao Fault (HGF; Fig. 2a), the ages of the granites in the area around the Haobugao Zn–Fe deposit (in the northeastern HGF area), the Hashitu molybdenum deposit (in the central HGF area) and the Huanggangliang Sn–Fe deposit (in the southwestern HGF area) are 146–140 Ma, 147–143 Ma (Zhai *et al.* 2014a) and 139 Ma (Zhou *et al.* 2012), respectively. The magmatism in the SGXR (Wang *et al.* 2006; Zhang *et al.* 2008a,b, 2010b) and the associated porphyry- and skarn-type deposits (132–139 Ma) (Zeng *et al.* 2010, 2011; Shu *et al.* 2013a; W. Mei, unpub. Ph.D. thesis, China Univ. Geosciences, 2014; Zhai *et al.* 2014b) and hydrothermal vein-type deposits (135–143 Ma) (Liu *et al.* 2010; Ouyang *et al.* 2013; Ruan *et al.* 2015) defined a widespread magmatic-metallogenic event created in Early Cretaceous time (~140 Ma).

The lead isotope compositions of the samples from the study area vary within a narrow range. The majority of the sulfides plot between the mantle evolution line and the orogenic evolution line, while only a small number of samples plot between the mantle and upper crust evolution lines (Fig. 12) (Zartman & Doe, 1981; Canals & Cardellach, 1997; Hou *et al.* 2004; Jiang *et al.* 2006). The similar Pb isotope compositions of the sulfides from the Haobugao deposit and those of other deposits in the SGXR indicate that they have similar lead sources (Ouyang *et al.* 2015). Furthermore, most of the samples plot within the field of the Mesozoic granitic rocks in the SGXR. The sulfides from the Haobugao deposit are more similar to those from the biotite monzogranite than those from the syenogranites (Fig. 12). In addition, the FeO^T (wt %), Cu (ppm) and Zn (ppm) contents of the sulfides in the biotite monzogranite (1.79–3.99, 5.97–185 and 75.4–366, respectively) are much higher than those in syenogranite (0.82–0.92, 2.41–2.63 and 36.38–37.86, respectively), suggesting that the biotite monzogranite can supply more ore-forming elements (Fe–Zn–Pb–Cu) than the syenogranite.

6.b.2. Apatite compositional constraints on the fertile and barren rocks in the Wulanba granite

The presence of redox-sensitive elements such as Mn, As, Fe, S, Eu and Ce in various oxidation states in the apatite may be related to the redox conditions of the host magma (Sha & Chappell, 1999; Prowatke & Klemme, 2006; Konecke *et al.* 2017). As the available As, Fe, Ce and Eu data were limited, the Mn content of the apatite was used to evaluate the oxygen fugacity of the magma. Because apatite crystallizes prior to other Mn-bearing minerals, the crystallization of other Mn-bearing minerals would not significantly influence Mn partitioning between the apatite and the melt (Xie *et al.* 2018). Apatite has an elevated Mn content at low oxygen fugacities at which manganese primarily exists as Mn^{2+} (Zhong *et al.* 2018). Miles *et al.* (2014) explored the use of the Mn concentration of apatite, which varies linearly and negatively with $\log f\text{O}_2$ ($\log f\text{O}_2 = -0.0022(\pm 0.0003)\text{Mn (ppm)} - 9.75(\pm 0.46)$), as an oxybarometer in intermediate and felsic igneous rocks. On the plot of $\log f\text{O}_2$ versus T (Fig. 13a), the apatite grains from the biotite monzogranite and syenogranite plot between the magnetite–haematite (MH) and NiNiO (NNO) buffers, indicating the apatite crystallized from a melt with a high oxygen fugacity. This is

also supported by the negative Ce anomalies of the magnetite, which indicates an oxidized ore-fluid (Liu *et al.* 2017). The calculated $\log f\text{O}_2$ values of the syenogranite range from -10.9 to -14.4 , while those of the biotite monzogranite range from -9.8 to -11.9 (Figs 6, 13b) (Miles *et al.* 2014). This indicates that compared to the barren syenogranite, the fertile biotite monzogranite is more oxidized. From the centre to the edge of the apatite grains from the biotite monzogranite (Fig. 6), the $\log f\text{O}_2$ values increase, indicating that the oxygen fugacity of the magma increased during apatite crystallization. It is generally agreed that compared to reduced magmas, oxidized magmas facilitate skarn mineralization (Li *et al.* 2017), because at higher oxygen fugacities, magmatic sulfur exists mainly as sulfate (SO_4^{2-}), which is more soluble in silicate melts than sulfide and tends to delay or even prevent the saturation of magmatic sulfide phases (Ballard *et al.* 2002; Richards, 2003). Zhong *et al.* (2018) also concluded that in the Weibao Cu–Pb–Zn skarn deposit, the ore-bearing intrusions are significantly more oxidized than the barren diorite porphyry. These results suggest that oxygen fugacity can potentially be used to differentiate between fertile and barren rocks.

Another key factor that may affect the production of magmas is the abundance of halogens (F and Cl), which can effectively complex and transport metals (Piccoli & Candela, 1994; Coulson *et al.* 2001; Webster *et al.* 2004, 2009). Apatite is a sensitive indicator of volatile composition (Boudreau *et al.* 1986; Mathez & Webster, 2005; Doherty *et al.* 2014). The calculated F concentrations of the source magmas (Mathez & Webster, 2005) of fertile (0.83–1.10 wt %) and barren rocks (0.82–1.01 wt %) are high but indistinguishable. In contrast, the calculated Cl concentrations of the source magmas (Mathez & Webster, 2005) of fertile (0.00625–0.01000 wt %) and barren rocks (0.00625–0.02125 wt %) are lower and differ significantly. Thus, the average F/Cl ratio of the source magma that produces fertile rocks (~123.45) is much higher than that of barren rocks (~73.98; Fig. 13c). The F/Cl ratio of fresh apatite reflects the ratio of the system it crystallized from because apatite is not vulnerable to subsolidus halogen exchange (Tacker & Stormer, 1989). Thus, our results provide indirect evidence that the F/Cl ratios of the parental magmas of fertile and barren rocks differ. The apatite grains from the Wulanba granite plot in the Cu–Zn–Pb skarn deposit field in Figure 13d. It can be seen that the Cl contents of the apatite in Cu–Pb–Zn skarn deposits are much lower than those of the apatite in typical porphyry Cu deposits (mostly >0.9 wt %), but their F contents are slightly higher, indicating that the high Cl content of the magma may have a greater influence on porphyry Cu deposits than on Cu–Pb–Zn skarn deposits. These results indicate that the $\log f\text{O}_2$ and F/Cl ratios (or Cl contents) of apatite may be used to distinguish between fertile and barren rocks, i.e. apatite can be used as an indicator of the mineralization potential.

7. Conclusions

In Early Cretaceous time, the Wulanba granite was produced by partial melting of juvenile crust derived from the depleted mantle with minor inputs of older crust in an extensional setting as a result of lithosphere delamination and asthenosphere upwelling, after which the magma was highly differentiated to produce an I-type granite. The Wulanba granite was most likely derived from a Late Neoproterozoic to Early Palaeozoic source during an important stage of crustal growth in the area.

Based on geological evidence from drill cores, the geochronology of the mineralization and the abundance of ore-forming elements

(Fe–Zn–Pb–Cu) in the biotite monzogranite, the biotite monzogranite contributed to the mineralization. Based on the geochemical characteristics of the apatite, the fertile biotite monzogranite has higher $\log f_{\text{O}_2}$ values and F/Cl ratios than the barren syenogranite, indicating that it can be regarded as an indicator of mineralization potential.

Acknowledgements. This research was financially supported by the National Key R&D Program of China (2017YFC0601303), the CAGS Research Fund (YYWF201715), the NSFC (41873051), and the Basic Work Program for Science and Technology (2014FY121000). We thank Professor Daming Bai from the Institute of Mineral Resources, CAGS for his assistance with the fieldwork. We are deeply indebted to the management of the Shandong Gold Group Co. Ltd for their permission to investigate and sample the Haobugao Fe–Zn deposit.

Supplementary material. To view supplementary material for this article, please visit <https://doi.org/10.1017/S0016756819000876>.

References

- Amelin Y, Lee DC, Halliday AN and Pidgeon RT (1999) Nature of the earth's earliest crust from hafnium isotopes in single detrital zircon. *Nature* **399**, 252–5.
- Ballard JR, Palin MJ and Campbell IH (2002) Relative oxidation states of magmas inferred from Ce(IV)/Ce(III) in zircon: application to porphyry copper deposits of northern Chile. *Contributions to Mineralogy and Petrology* **144**, 347–64.
- Ballouard C, Poujol M, Bouvais P, Branquet Y, Tartèse R and Vigneresse JL (2016) Nb–Ta fractionation in peraluminous granites: a marker of the magmatic-hydrothermal transition. *Geology* **44**, 231–4.
- Bonin B (2007) A-type granites and related rocks: evolution of a concept, problems and prospects. *Lithos* **97**, 1–29.
- Boudreau AE, Mathez EA and McCallum IS (1986) Halogen geochemistry of the Stillwater and Bushveld Complexes: evidence for transport of the platinum-group elements by Cl-rich fluids. *Journal of Petrology* **27**, 967–86.
- Cai JH, Yan GH, Xiao CD, Wang GY, Mu BL and Zhang RH (2004) Nd, Sr, Pb isotopic characteristics of the Mesozoic intrusive rocks in the Taihang–Da Hinggan Mountains tectonomagmatic belt and their source region. *Acta Petrologica Sinica* **20**, 1225–42.
- Canals A and Cardellach E (1997) Ore lead and sulphur isotope pattern from the low temperature veins of the Catalan Coastal Ranges (NE Spain). *Mineralium Deposita* **32**, 243–9.
- Chakhmouradian AR, Reguir EP, Zaitsev AN, Couëslan C, Xu C, Kynický J, Mumin AH and Yang P (2017) Apatite in carbonatitic rocks: compositional variation, zoning, element partitioning and petrogenetic significance. *Lithos* **274**, 188–213.
- Chappell BW (1999) Aluminium saturation in I- and S- type granites and the characterization of fractionated haplogranites. *Lithos* **46**, 535–51.
- Chappell BW, Bryant CJ, Wyborn D, White AJR and Williams IS (1998) High- and low temperature I-type granites. *Resource Geology* **48**, 225–35.
- Chappell BW and White AJR (2001) Two contrasting granite types: 25 years later. *Australian Journal of Earth Sciences* **48**, 489–99.
- Chen YJ and Fu SG (1992) *Mineralization of Gold Deposits in West Henan, China*. Beijing: China Seismological Press, 234 pp. (in Chinese with English abstract).
- Chen B, Jahn BM, Simon W and Xu B (2000) Two contrasting Paleozoic magmatic belts in northern Inner Mongolia, China: petrogenesis and tectonic implications. *Tectonophysics* **328**, 157–82.
- Chen YJ, Pirajno F and Qi JP (2005) Origin of gold metallogeny and sources of ore-forming fluids, Jiaodong province, eastern China. *International Geology Review* **47**, 530–49.
- Chen L, Yan Z, Wang ZQ and Wang KM (2017) Characteristics of apatite from 160–140 Ma Cu(Mo) and Mo(W) deposits in East Qinling. *Acta Geologica Sinica* **91**, 1925–42 (in Chinese with English abstract).
- Chu XL, Huo WG and Zhang X (2001) Sulfur, carbon and lead isotope studies of the Dajing polymetallic deposit in Linxi county, Inner Mongolia, China — implication for metallogenic elements from hypomagmatic source. *Resource Geology* **51**, 333–44.
- Claiborne LL, Miller CF, Walker BA, Wooden JL, Mazdab FK and Bea F (2006) Tracking magmatic processes through Zr/Hf ratios in rocks and Hf and Ti zoning in zircons: an example from the Spirit Mountain batholith, Nevada. *Mineralogical Magazine* **70**, 517–43.
- Coulson IM, Dipple GM and Raudsepp M (2001) Evolution of HF and HCl activity in magmatic volatiles of the gold-mineralized Emerald Lake pluton, Yukon Territory, Canada. *Mineralium Deposita* **36**, 594–606.
- Defant MJ and Drummond MS (1990) Derivation of some modern arc magmas by melting of young subducted lithosphere. *Nature* **347**, 662–5.
- Ding T, Ma D, Lu JJ and Zhang R (2015) Apatite in granitoids related to polymetallic mineral deposits in southeastern Hunan province, Shi–Hang zone, China: implications for petrogenesis and metallogenesis. *Ore Geology Reviews* **69**, 104–17.
- Doherty AL, Webster JD, Goldoff BA and Piccoli PM (2014) Partitioning behavior of chlorine and fluorine in felsic melt–fluid(s)–apatite systems at 50 MPa and 850–950 °C. *Chemical Geology* **384**, 94–109.
- Ehrlou S, Belousova E, Griffin WL, Pearson NJ and O'Reilly SY (2006) Trace element and isotopic composition of GJ-red zircon standard by laser ablation. *Geochimica et Cosmochimica Acta* **70**, A158.
- Ellis DJ and Thompson AB (1986) Subsolvus and partial melting reactions in the quartz excess CaO–MgO–Al₂O₃–SiO₂–H₂O system under water-excess and water deficient conditions to 10 kb: some implications for the origin of peraluminous melts from mafic rocks. *Journal of Petrology* **27**, 91–121.
- Eugster HP and Wones DR (1962) Stability relations of the ferruginous biotite, Annite. *Journal of Petrology* **3**, 82–9.
- Fujimaki H (1986) Partition coefficients of Hf, Zr, and REE between zircon, apatite and liquid. *Contributions to Mineralogy and Petrology* **94**, 42–5.
- Gao S, Rudnick RL, Carlson RW, McDonough WF and Liu YS (2002) Re–Os evidence for replacement of ancient mantle lithosphere beneath the North China craton. *Earth and Planetary Science Letters* **198**, 307–22.
- Gelman SE, Deering CD, Bachmann O, Huber C and Gutiérrez FJ (2014) Identifying the crystal graveyards remaining after large silicic eruptions. *Earth and Planetary Science Letters* **403**, 299–306.
- Green TH (1980) Island arc and continent-building magmatism: a review of petrogenetic models based on experimental petrology and geochemistry. *Tectonophysics* **63**, 367–85.
- Guo F, Fan WM, Gao XF, Li CW, Miao LC, Zhao L and Li HX (2010) Sr–Nd–Pb isotope mapping of Mesozoic igneous rocks in NE China: constraints on tectonic framework and Phanerozoic crustal growth. *Lithos* **120**, 563–78.
- Guo F, Fan WM, Li CW, Gao XF and Miao LC (2009) Early Cretaceous highly positive ϵ_{Nd} felsic volcanic rocks from the Hinggan Mountains, NE China: origin and implications for Phanerozoic crustal growth. *International Journal of Earth Sciences* **98**, 1395–411.
- Halliday AN, Davidson JP, Hildreth W and Holden P (1991) Modelling the petrogenesis of high Rb/Sr silicic magmas. *Chemical Geology* **92**, 107–14.
- Han G, Liu Y, Neubauer F, Johann G, Zhao Y, Wen Q, Li W, Wu L, Jiang X and Zhao L (2012) Provenance analysis of Permian sandstones in the central and southern Da Xing'an mountains, China: constraints on the evolution of the eastern segment of the Central Asian Orogenic Belt. *Tectonophysics* **580**, 100–13.
- Han BF, Wang SG, Jahn BM, Hong DW, Kagami H and Sun YL (1997) Depleted mantle source for the Ulungur river A-type granites from North Xinjiang, China: geochemistry and Nd–Sr isotopic evidence, and implications for Phanerozoic crustal growth. *Chemical Geology* **138**, 135–59.
- Heinhost J, Lehmann B, Ermolov P, Serykh V and Zhurutin S (2000) Paleozoic crustal growth and metallogeny of Central Asia: evidence from magmatic-hydrothermal ore system of Central Kazakhstan. *Tectonophysics* **328**, 69–87.
- Hong DW, Wang SG, Xie XL and Zhang JS (2000) Genesis of positive ϵ_{Nd} (t) granitoids in the Great Hinggan Range–Mongolia orogenic belt and growth continental crust. *Earth Science Frontiers* **7**, 441–56 (in Chinese with English abstract).
- Hou ML, Ding X and Jiang SY (2004) Lead and sulfur isotope geochemistry of the Hexi Gold deposit in Penglai Eastern Shandong. *Acta Geoscientica Sinica* **25**, 145–50 (in Chinese with English abstract).

- Hou KJ, Li YH and Tian YY (2009) *In situ* U–Pb zircon dating using laser ablation–multi ion counting–ICP–MS. *Mineral Deposits* **28**, 481–92 (in Chinese with English abstract).
- Hou KJ, Li YH, Zhou TR, Qu XM, Shi YR and Xie GQ (2007) Laser ablation–MC–ICP–MS technique for Hf isotope microanalysis of zircon and its geological applications. *Acta Petrologica Sinica* **23**, 2595–604 (in Chinese with English abstract).
- Irber W (1999) The lanthanide tetrad effect and its correlation with K/Rb, Eu/Eup, Sr/Eu, Y/Ho, and Zr/Hf of evolving peraluminous granite suites. *Geochimica et Cosmochimica Acta* **63**, 489–508.
- Jahn BM (2004) The Central Asian Orogenic Belt and growth of the continental crust in the Phanerozoic. In *Aspects of the Tectonic Evolution of China* (eds J Malpas, CJN Fletcher, JR Ali and JC Aitchison), pp. 73–100. Geological Society of London, Special Publication no. 226.
- Jahn BM, Capdevila R, Liu DY, Vernon A and Badarch G (2004) Sources of Phanerozoic granitoids in the transect Bayanhongor–Ulaan Baatar, Mongolia: geochemical and Nd isotopic evidence, and implications for Phanerozoic crustal growth. *Journal of Asian Earth Sciences* **23**, 629–53.
- Jahn BM, Wu FY, Capdevila R, Fourcade S, Wang YX and Zhao ZH (2001) Highly evolved juvenile granites with tetrad REE patterns: the Woduhe and Baerzhe granites from the Great Xing'an (Khangin) Mountains in NE China. *Lithos* **59**, 171–98.
- Jahn BM, Wu FY and Chen B (2000a) Granitoids of the Central Asian Orogenic Belt and continental growth in the Phanerozoic. *Transactions of the Royal Society of Edinburgh: Earth Sciences* **91**, 181–93.
- Jahn BM, Wu FY and Chen B (2000b) Massive granitoid generation in Central Asia: Nd isotopic evidence and implication for continental growth in the Phanerozoic. *Episodes* **23**, 82–92.
- Jia PP, Wei JH, Gong QW and Zhao WL (2011) Analysis of geological background and ore-searching prospect for the copper–molybdenum deposits in the Da Hingan Ling area. *Geology and Exploration* **47**, 151–62 (in Chinese with English abstract).
- Jiang SH, Chen CL, Bagas L, Liu Y, Han N, Kang H and Wang ZH (2017) Two mineralization events in the Baiyinnuoer Zn–Pb deposit in Inner Mongolia, China: evidence from field observations, S–Pb isotopic compositions and U–Pb zircon ages. *Journal of Asian Earth Sciences* **144**, 339–67.
- Jiang SH, Liang QL, Liu YF and Liu Y (2012) Zircon U–Pb ages of magmatic rocks occurring in around the Dajing Cu–Ag–Sn polymetallic deposit of Inner Mongolia constrains to the ore-forming age. *Acta Petrologica Sinica* **28**, 495–513 (in Chinese with English abstract).
- Jiang SH, Nie FJ, Bai DM, Liu YF and Liu Y (2011a) Geochronology evidence for Indosinian mineralization in Baiyinnuoer Pb–Zn deposit of Inner Mongolia. *Mineral Deposits* **30**, 787–98 (in Chinese with English abstract).
- Jiang SH, Nie FJ, Liu YF, Hou WR, Bai DM, Liu Y and Liang QL (2011b) Geochronology of intrusive rocks occurring in and around the Mengentaolegai Ag–polymetallic deposit, Inner Mongolia. *Journal of Jilin University (Earth Sciences Edition)* **41**, 1755–69 (in Chinese with English abstract).
- Jiang SH, Nie FJ, Liu YF and Yun F (2010) Sulfur and lead isotopic compositions of Bairendaba and Weilasituo silver–polymetallic deposits, Inner Mongolia. *Mineral Deposits* **28**, 101–12 (in Chinese with English abstract).
- Jiang SY, Yang T, Li L, Zhao KD and Ling HF (2006) Lead and sulfur isotopic compositions of sulfides from the TAG hydrothermal field, Mid-Atlantic Ridge. *Acta Petrologica Sinica* **22**, 2597–602 (in Chinese with English abstract).
- Jiang SH, Zhang LL, Liu YF, Liu CH, Kang H and Wang FX (2018) Metallogeny of Xing-Meng Orogenic Belt and some related problems. *Mineral Deposits* **37**, 671–711 (in Chinese with English abstract).
- King PL, Chappell BW, Allen CM and White AJR (2001) Are A-type granites the high-temperature felsic granites? Evidence from fractionated granites of the Wangrah Suite. *Journal of the Geological Society of Australia* **48**, 501–14.
- Konecke BA, Fiege A, Simon AC, Parat F and Stechern A (2017) Co-variability of S₆₊, S₄₊, and S₂₋ in apatite as a function of oxidation state: implications for a new oxybarometer. *American Mineralogist* **102**, 548–57.
- Kovalenko VI, Yarmolyuk VV, Kovach VP, Kotov AB, Kozakov IK and Sal'nikova EB (1996) Sources of Phanerozoic granitoids in Central Asia: Sm–Nd isotope data. *Geochemical International* **34**, 628–40.
- Li JW, Bi SY, Selby D, Chen L, Vasconcelos P, Thiede D, Zhou MF, Zhao XF, Li ZK and Qiu HN (2012) Giant Mesozoic gold provinces related to the destruction of the North China Craton. *Earth and Planetary Science Letters* **349–350**, 26–37.
- Li X, Chi G, Zhou Y, Deng T and Zha J (2017) Oxygen fugacity of Yanshanian granites in South China and implications for metallogeny. *Ore Geology Reviews* **88**, 690–701.
- Li XH, Li WX and Li ZX (2007) On the genetic classification and tectonic implications of the Early Yanshanian granitoids in the Nanling Range, South China. *China Science Bulletin* **52**, 984–91 (in Chinese with English abstract).
- Li JZ, Qin KZ, Li GM, Ishihara S, Jin LY, Song GX and Meng ZJ (2014a) Formation of the giant Chalukou porphyry Mo deposit in northern Great Xing'an Range, NE China: partial melting of the juvenile lower crust in intra-plate extensional environment. *Lithos* **202–203**, 138–56.
- Li JF, Wang KY, Quan HY, Sun FY, Zhao LS and Zhang XB (2016) Discussion on the magmatic evolution sequence and metallogenic geodynamical setting background Hongling Pb–Zn deposit in the southern Da Xing'an Mountains. *Acta Petrologica Sinica* **32**, 1529–42 (in Chinese with English abstract).
- Li PZ and Yu JS (1993) Nianzishan miarolitic alkaline granite stock, Heilongjiang—its ages and geological implications. *Geochimica* **22**, 389–98 (in Chinese with English abstract).
- Li Y, Zhou H, Brouwer FM, Xiao W, Wijbrans JR and Zhong Z (2014b) Early Paleozoic to Middle Triassic divergent accretion in the Central Asian Orogenic Belt: insights from zircon U–Pb dating of ductile shear zones in central Inner Mongolia, China. *Lithos* **205**, 84–111.
- Lin Q, Ge WC, Wu FY, Sun DY and Cao L (2004) Geochemistry of Mesozoic granites in Da Hinggan Ling ranges. *Acta Petrologica Sinica* **20**, 403–12 (in Chinese with English abstract).
- Liu YF, Jiang SH and Bagas L (2016) The genesis of metal zonation in the Weilasituo and Bairendaba Ag–Zn–Pb–Cu–(Sn–W) deposits in the shallow part of a porphyry Sn–W–Rb system, Inner Mongolia, China. *Ore Geology Reviews* **75**, 150–73.
- Liu Y, Jiang SH, Bagas L, Han N, Chen CL and Kang H (2017) Isotopic (C–O–S) geochemistry and Re–Os geochronology of the Haobugao Zn–Fe deposit in Inner Mongolia, NE China. *Ore Geology Reviews* **82**, 130–47.
- Liu YF, Jiang SH and Zhang Y (2010) The SHRIMP zircon U–Pb dating and geological features of Bairendaba diorite in the Xilinhaote area, Inner Mongolia, China. *Geological Bulletin of China* **29**, 688–96 (in Chinese with English Abstract).
- Liu W, Pan XF, Xie LW and Li H (2007) Sources of material for the Linxi granitoids, the southern segment of the Da Hinggan Mts.: when and how continental crust grew? *Acta Petrologica Sinica* **23**, 441–60 (in Chinese with English abstract).
- Liu W, Siebel W, Li XJ and Pan XF (2005) Petrogenesis of the Linxi granitoids, northern Inner Mongolia of China: constraints on basaltic underplating. *Chemical Geology* **219**, 5–35.
- Liu LJ, Zhou TF, Zhang DY, Yuan F, Liu GX, Zhao ZC, Sun JD and White N (2018) S isotopic geochemistry, zircon and cassiterite U–Pb geochronology of the Haobugao Sn polymetallic deposit, southern Great Xing'an Range, NE China. *Ore Geology Reviews* **93**, 168–80.
- Ludwig KR (2003). *User's Manual for Isoplot 3.00: A Geochronological Toolkit for Microsoft Excel*. Berkeley: Berkeley Geochronology Center Special Publication no. 4.
- Mao JW, Wang YT, Lehmann B, Yu JJ, Du AD, Mei YX, Li YT, Zang WS, Stein HJ and Zhou TF (2006) Molybdenite Re–Os and albite ⁴⁰Ar/³⁹Ar dating of Cu–Au–Mo and magnetite porphyry systems in the Yangtze River valley and metallogenic implications. *Ore Geology Reviews* **29**, 307–24.
- Mao JW, Xie GQ, Bierlein F, Qu WJ, Du AD, Ye HS, Pirajno F, Li HM, Guo BJ, Lie YF and Yang ZQ (2008) Tectonic implications from Re–Os dating of

- Mesozoic molybdenum deposits in the East Qinling–Dabie orogenic belt. *Geochimica et Cosmochimica Acta* **72**, 4607–26.
- Mao JW, Xie GQ, Pirajno F, Ye HS, Wang YB, Li YF, Xiang JF and Zhao HJ** (2010) Late Jurassic–Early Cretaceous granitoid magmatism in East Qinling, central-eastern China: SHRIMP zircon U–Pb ages and tectonic implications. *Australian Journal of Earth Sciences* **57**, 51–78.
- Mao JW, Xie GQ, Zhang ZH, Li XF, Wang YT, Zhang CQ and Li YF** (2005) Mesozoic large-scale metallogenic pulses in North China and corresponding geodynamic settings. *Acta Petrologica Sinica* **21**, 169–88 (in Chinese with English abstract).
- Marks MA, Wenzel T, Whitehouse MJ, Loose M, Zack T, Barth M, Barth M, Worgard L, Krasz V, Eby GN, Stosnach H and Markl G** (2012) The volatile inventory (F, Cl, Br, S, C) of magmatic apatite: an integrated analytical approach. *Chemical Geology* **291**, 241–55.
- Martin H** (1999) Adakitic magmas: modern analogues of Archaean granitoids. *Lithos* **46**, 411–29.
- Mathez EA and Webster JD** (2005) Partitioning behavior of chlorine and fluorine in the system apatite–silicate melt–fluid. *Geochimica et Cosmochimica Acta* **69**, 1275–86.
- Meng QR** (2003) What drove late Mesozoic extension of the northern China–Mongolia tract? *Tectonophysics* **369**, 155–74.
- Miles AJ, Graham CM, Hawkesworth CJ, Gillespie MR, Hinton RW and Bromiley GD** (2014) Apatite: a new redox proxy for silicic magmas? *Geochimica et Cosmochimica Acta* **132**, 101–19.
- Miller CF and Mittlefehldt DW** (1982) Depletion of light rare-earth elements in felsic magmas. *Geology* **10**, 129–33.
- Miller CF and Mittlefehldt DW** (1984) Extreme fractionation in felsic magma chambers: a product of liquid-state diffusion or fractional crystallization? *Earth and Planetary Science Letters* **68**, 151–8.
- Mitchell R, Chudy T, McFarlane CR and Wu FY** (2017) Trace element and isotopic composition of apatite in carbonatites from the Blue River area (British Columbia, Canada) and mineralogy of associated silicate rocks. *Lithos* **286–287**, 75–91.
- Nesbitt HW and Young GM** (1982) Early Proterozoic climates and plate motions inferred from major element chemistry of lutites. *Nature* **299**, 715–7.
- Nie FJ, Jiang SH, Su XX and Wang XL** (2002) Geological features and origin of gold deposits occurring in the Baotou–Bayan Obo district, south-central Inner Mongolia, People’s Republic of China. *Ore Geology Reviews* **30**, 1–29.
- Ouyang HG, Mao JW, Santosh M, Wu Y, Hou L and Wang XF** (2014) The Early Cretaceous Weilasituo Zn–Cu–Ag vein deposit in the southern Great Xing’an Range, northeast China: fluid inclusions, H, O, S, Pb isotope geochemistry and genetic implications. *Ore Geology Reviews* **56**, 503–15.
- Ouyang HG, Mao JW, Santosh M, Zhou J, Zhou ZH, Wu Y and Hou L** (2013) Geodynamic setting of Mesozoic magmatism in NE China and surrounding regions: perspectives from spatio-temporal distribution patterns of ore deposits. *Journal of Asian Earth Sciences* **78**, 222–36.
- Ouyang HG, Mao JW, Zhou ZH and Su HM** (2015) Late Mesozoic metallogeny and intracontinental magmatism, southern Great Xing’an Range, northeastern China. *Gondwana Research* **27**, 1153–72.
- Pan LC, Hu RZ, Wang XS, Bi XW, Zhu JJ and Li C** (2016) Apatite trace element and halogen compositions as petrogenetic–metallogenic indicators: examples from four granite plutons in the Sanjiang region, SW China. *Lithos* **254**, 118–30.
- Piccoli PM and Candela PA** (1994) Apatite in felsic rocks; a model for the estimation of initial halogen concentrations in the Bishop Tuff (Long Valley) and Tuolumne Intrusive Suite (Sierra Nevada Batholith) magmas. *American Journal of Science* **294**, 92–135.
- Poli GE and Tommasini S** (1991) Model for the origin and significance of microgranular enclaves in calc-alkaline granitoids. *Journal of Petrology* **32**, 657–66.
- Prowatke S and Klemme S** (2006) Trace element partitioning between apatite and silicate melts. *Geochimica et Cosmochimica Acta* **70**, 4513–27.
- Qiu JT, Yu XQ, Santosh M, Zhang DH, Chen SQ and Li PJ** (2013) Geochronology and magmatic oxygen fugacity of the Tongcun molybdenum deposit, northwest Zhejiang, SE China. *Mineralium Deposita* **48**, 545–56.
- Richards JP** (2003) Tectono-magmatic precursors for porphyry Cu–(MoAu) deposit formation. *Economic Geology* **98**, 1515–33.
- Ruan BX, Lv XB, Yang W, Liu ST, Yu YM, Wu CM and Munir MAA** (2015) Geology, geochemistry and fluid inclusions of the Bianjiadayuan Pb–Zn–Ag deposit, Inner Mongolia, NE China: implications for tectonic setting and metallogeny. *Ore Geology Reviews* **71**, 121–37.
- Rui ZY, Shi LD and Fang R** (1994) *Deposit Geology of the Non-ferrous Metal Deposits in the Northern Margin of North China and Adjacent Areas*. Beijing: Geological Publishing House, 476 pp. (in Chinese with English abstract).
- Scott JA, Humphreys MC, Mather TA, Pyle DM and Stock MJ** (2015) Insights into the behaviour of S, F, and Cl at Santiaguito Volcano, Guatemala, from apatite and glass. *Lithos* **232**, 375–94.
- Sha LK and Chappell BW** (1999) Apatite chemical composition, determined by electron microprobe and laser-ablation inductively coupled plasma mass spectrometry, as a probe into granite petrogenesis. *Geochimica et Cosmochimica Acta* **63**, 3861–81.
- Shao JA, Han QJ, Zhang LQ and Mu BL** (1999) Cumulate complex xenoliths in the Early Mesozoic eastern Inner Mongolia. *China Science Bulletin* **44**, 1272–9 (in Chinese with English abstract).
- Shao JA, Liu FT, Chen H and Han QJ** (2001) Relationship between Mesozoic magmatism and subduction in Da Hinggan – Yanshan area. *Acta Geologica Sinica* **75**, 56–63 (in Chinese with English abstract).
- Shao JA, Mu BL, Zhu HZ and Zhang LQ** (2010) Material source and tectonic settings of the Mesozoic mineralization of the Great Hinggan Range. *Acta Petrologica Sinica* **26**, 649–56 (in Chinese with English abstract).
- Sheng JF and Fu XZ** (1999) *Metallogenetic Environment and Geological Characteristics of Copper–Polymetallic Ore Deposits in Middle Part of Da Hinggan Mts*. Beijing: Seismological Publishing House (in Chinese).
- Shu QH, Lai Y, Sun Y, Wang C and Meng S** (2013a) Ore genesis and hydrothermal evolution of the Baiyinnuo’er zinc–lead skarn deposit, Northeast China: evidence from isotopes (S, Pb) and fluid inclusions. *Economic Geology* **108**, 835–60.
- Shu QH, Lai Y, Wang C, Xu JJ and Sun Y** (2013b) Geochronology, geochemistry and Sr–Nd–Hf isotopes of the Haisugou porphyry Mo deposit, northeast China, and their geological significance. *Journal of Asian Earth Sciences* **79**, 777–91.
- Sillitoe RH** (2010) Porphyry copper systems. *Economic Geology* **105**, 3–41.
- Sisson TW, Ratajeski K and Hankins WB** (2005) Voluminous granitic magmas from common basaltic sources. *Contributions to Mineralogy and Petrology* **148**, 635–61.
- Sun SS and McDonough WF** (1989) Chemical and isotopic systematics of oceanic basalts: implications for mantle composition and processes. In *Magmatism in the Ocean Basins* (eds AD Saunders and MJ Norry), pp. 313–45. Geological Society of London, Special Publication no. 42.
- Sun DY, Wu FY, Li HM and Lin Q** (2001) Emplacement age of the post-orogenic A-type granites in northwestern Lesser Xing’an Ranges, and its relationship to the eastward extension of Suolunshan–Hegenshan–Zhalaithe collisional suture zone. *China Science Bulletin* **46**, 427–32 (in Chinese with English abstract).
- Tacker RC and Stormer JC** (1989) A thermodynamic model for apatite solid solutions, applicable to high-temperature geologic problems. *American Mineralogist* **74**, 877–88.
- Taylor SR and McLennan SM** (1985) *The Continental Crust: Its Composition and Evolution*. Oxford: Blackwell Scientific Publications, 312 pp.
- Tepley FJ, Davidson JP, Tilling RI and Arth JG** (2000) Magma mixing, recharge and eruption histories recorded in plagioclase phenocrysts from El Chichon Volcano, Mexico. *Journal of Petrology* **41**, 1397–411.
- Wang CY** (2015) Lead-zinc polymetallic metallogenic series and prospecting direction of Huanggangliang – Ganzhuermiao metallogenic belt, Inner Mongolia. Ph.D. thesis, Jilin University, Changchun, China. Published thesis.
- Wang XD, Xu DM, Lv XB, Wei W, Mei W, Fan XJ and Sun BK** (2018) Origin of the Haobugao skarn Fe–Zn polymetallic deposit, Southern Great Xing’an Range, NE China: geochronological, geochemical, and Sr–Nd–Pb isotopic constraints. *Ore Geology Reviews* **94**, 58–72.

- Wang Q, Xu JF, Zhao ZH, Bao ZW, Xu W and Xiong XL (2004) Cretaceous high potassium intrusive rocks in the Yueshan–Hongzhen area of east China: adakites in an extensional tectonic regime within a continent. *Geochemical Journal* **38**, 417–34.
- Wang YX and Zhao ZH (1997) Geochemistry and origin of the Baerzhe REE–Nb–Be–Zr superlarge deposit. *Geochimica* **26**, 24–35 (in Chinese with English abstract).
- Wang F, Zhou XH, Zhang LC, Ying JF, Zhang YT, Wu FY and Zhu RX (2006) Late Mesozoic volcanism in the Great Xing'an Range (NE China): timing and implications for the dynamic setting of NE Asia. *Earth and Planetary Science Letters* **251**, 179–98.
- Watson BE and Green HT (1981) Apatite/liquid partition coefficients for the rare earth elements and strontium. *Earth and Planetary Science Letters* **56**, 405–21.
- Watson BE and Harrison MT (1983) Zircon saturation revisited: temperature and composition effects in a variety of crustal magma types. *Earth and Planetary Science Letters* **64**, 295–304.
- Webster JD, Tappen CM and Mandeville CW (2009) Partitioning behavior of chlorine and fluorine in the system apatite–melt–fluid. II: felsic silicate systems at 200 MPa. *Geochimica et Cosmochimica Acta* **73**, 559–81.
- Webster J, Thomas R, Förster HJ, Seltmann R and Tappen C (2004) Geochemical evolution of halogen-enriched granite magmas and mineralizing fluids of the Zinnwald tin-tungsten mining district, Erzgebirge, Germany. *Mineralium Deposita* **39**, 452–72.
- Whalen JB, Currie KL and Chappell BW (1987) A-type granites: geochemical characteristics, discrimination and petrogenesis. *Contributions to Mineralogy and Petrology* **95**, 407–19.
- Windley BF, Alexeiev D, Xiao WJ, Kröner A and Badarch G (2007) Tectonic models for accretion of the Central Asian Orogenic Belt. *Journal of the Geological Society, London* **164**, 31–47.
- Wu FY, Jahn BM, Wilde SA, Lo CH, Yui TF, Lin Q, Ge WC and Sun DY (2003) Highly fractionated I-type granites in NE China (II): isotopic geochemistry and implications for crustal growth in the Phanerozoic. *Lithos* **67**, 191–204.
- Wu FY, Jahn BM, Wilde SA and Sun DY (2000) Phanerozoic crustal growth: U–Pb and Sr–Nd isotopic evidence from the granites in northeastern China. *Tectonophysics* **328**, 89–113.
- Wu FY, Lin JQ, Wilde SA, Zhang XO and Yang JH (2005) Nature and significance of the Early Cretaceous giant igneous event in eastern China. *Earth and Planetary Science Letters* **233**, 103–19.
- Wu FY, Sun DY, Li HM, Jahn BM and Wilde SA (2002) A-type granites in northeastern China: age and geochemical constraints on their petrogenesis. *Chemical Geology* **187**, 143–73.
- Wu FY, Sun DY, Li HM and Wang XL (2001) The nature of basement beneath the Songliao Basin in NE China: geochemical and isotopic constraints. *Physics and Chemistry of the Earth, Part A* **26**, 793–803.
- Wu FY, Sun DY and Lin Q (1999) Petrogenesis of the Phanerozoic granites and crustal growth in Northeast China. *Acta Petrologica Sinica* **15**, 181–9 (in Chinese with English abstract).
- Wu HY, Zhang LC, Wan B, Chen ZG, Xiang P, Pirajno F, Du AD, Qu WJ and Wu HY (2011a) Re–Os and $^{40}\text{Ar}/^{39}\text{Ar}$ ages of the Jiguanshan porphyry Mo deposit, Xilamulun metallogenic belt, NE China, constraints on mineralization events. *Mineralium Deposita* **46**, 171–85.
- Wu HY, Zhang LC, Wan B, Chen ZG, Zhang XJ and Xiang P (2011b) Geochronological and geochemical constraints on Aolunhua porphyry Mo–Cu deposit, northeast China, and its tectonic significance. *Ore Geology Reviews* **43**, 78–91.
- Xiao WJ, Windley BF, Huang BC, Han CM, Yuan C, Chen HL, Sun M, Sun S and Li JL (2009) End-Permian to mid-Triassic termination of the accretionary processes of the southern Altaids: implications for the geodynamic evolution, Phanerozoic continental growth, and metallogeny of Central Asia. *International Journal of Earth Sciences* **98**, 1189–217.
- Xiao CD, Zhang ZL and Zhao LQ (2004) Nd, Sr and Pb isotope geochemistry of Yanshanian granitoids in eastern Inner Mongolia and their origins. *Geology in China* **31**, 57–63 (in Chinese with English abstract).
- Xie F, Tang J, Chen Y and Lang X (2018) Apatite and zircon geochemistry of Jurassic porphyries in the Xiongcuo district, southern Gangdese porphyry copper belt: implications for petrogenesis and mineralization. *Ore Geology Reviews* **96**, 98–114.
- Xu B, Charvet J, Chen Y, Zhao P and Shi G (2012) Middle Paleozoic convergent orogenic belts in western Inner Mongolia (China): framework, kinematics, geochronology and implications for tectonic evolution of the Central Asian Orogenic Belt. *Gondwana Research* **23**, 1342–64.
- Xu WL, Pei FP, Wang F, Meng E, Ji WQ, Yang DB and Wang W (2013) Spatial–temporal relationships of Mesozoic volcanic rocks in NE China: constraints on tectonic overprinting and transformations between multiple tectonic regimes. *Journal of Asian Earth Sciences* **74**, 167–93.
- Zartman RE and Doe BR (1981) Plumbotectonics—the model. *Tectonophysics* **75**, 135–62.
- Zeng QD, Liu JM, Chu SX, Wang YB, Sun Y, Duan XX, Zhou LL and Qu WJ (2013) Re–Os and U–Pb geochronology of the Duobaoshan porphyry Cu–Mo–(Au) deposit, northeast China, and its geological significance. *Journal of Asian Earth Sciences* **79**, 895–909.
- Zeng QD, Liu JM, Yu CM, Ye J and Liu HT (2011) Metal deposits in the Da Hinggan Mountains, NE China styles, characteristics, and exploration potential. *International Geology Review* **53**, 846–78.
- Zeng QD, Liu JM and Zhang ZL (2010) Re–Os geochronology of porphyry molybdenum deposit in south segment of Da Hinggan Mountains, northeast China. *Journal of Earth Science* **21**, 392–401.
- Zhai DG, Liu JJ, Wang JP, Yang YQ, Zhang HY, Wang XL, Zhang QB, Wang GW and Liu ZJ (2014a) Zircon U–Pb and molybdenite Re–Os geochronology, and whole-rock geochemistry of the Hashitu molybdenum deposit and host granitoids, Inner Mongolia, NE China. *Journal of Asian Earth Sciences* **79**, 144–60.
- Zhai DG, Liu JJ, Wang JP, Yao MJ, Wu SH, Fu C, Liu ZJ, Wang SG and Li YX (2013) Fluid evolution of the Jiawula Ag–Pb–Zn deposit, Inner Mongolia: mineralogical, fluid inclusion, and stable isotopic evidence. *International Geology Review* **55**, 204–24.
- Zhai DG, Liu JJ and Zhang HY (2014b) S–Pb isotopic geochemistry, U–Pb and Re–Os geochronology of the Huanggangliang Fe–Sn deposit, Inner Mongolia, NE China. *Ore Geology Reviews* **59**, 109–22.
- Zhang D, Ai X and Bao X (1994) Nonferrous metallic deposits in Huanggang Ganzhuermiao Mesozoic reworking region. In *Geology and Nonferrous Metallic Deposits in the Northern Margin of the North China Block and Its Adjacent Area* (ed. Z Rui), pp. 314–63. Beijing: Geological Publishing House.
- Zhang JH, Gao S, Ge WC, Wu FY, Yang JH, Wilde SA and Li M (2010a) Geochronology of the Mesozoic volcanic rocks in the Great Xing'an Range, northeastern China: implications for subduction-induced delamination. *Chemical Geology* **276**, 144–65.
- Zhang JH, Ge WC, Wu FY, Wilde SA, Yang JH and Liu XM (2008a) Large-scale Early Cretaceous volcanic events in the northern Great Xing'an Range, northeastern China. *Lithos* **102**, 138–57.
- Zhang C, Sun W, Wang J, Zhang L, Sun S and Wu K (2017) Oxygen fugacity and porphyry mineralization: a zircon perspective of Dexing porphyry Cu deposit, China. *Geochimica et Cosmochimica Acta* **206**, 343–63.
- Zhang M, Zhai YS, Shen CL, Liu YH, Yang SS, Zhai DG, Yao MJ, Wang JP, Wang SG, Gao ZX and Zhang L (2011) Metallogenic system of copper polymetallic deposits in the middle-southern part of Da Hinggan Mountains, China. *Geoscience* **25**, 819–31.
- Zhang XJ, Zhang LC, Jin XD, Wu HY, Xiang P and Chen ZG (2010b) U–Pb ages, geochemical characteristics and their implications of Banlashan molybdenum deposit. *Acta Petrologica Sinica* **26**, 1411–22.
- Zhang L, Zhou X, Ying J, Wang F, Guo F, Wan B and Chen Z (2008b) Geochemistry and Sr–Nd–Pb–Hf isotopes of Early Cretaceous basalts from the Great Xinggan Range, NE China: implications for their origin and mantle source characteristics. *Chemical Geology* **256**, 12–23.
- Zhao YM and Zhang DQ (1997) *Metallogeny and Prospective Evaluation of Copper Polymetallic Deposits in the Da Hinggan Mountains and Surrounding Regions*. Beijing: Seismic Publisher (in Chinese).

- Zhong SH, Feng CY, Seltmann R, Li DX and Dai ZH** (2018) Geochemical contrasts between Late Triassic ore-bearing and barren intrusions in the Weibao Cu–Pb–Zn deposit, East Kunlun Mountains, NW China: constraints from accessory minerals (zircon and apatite). *Mineralium Deposita* **53**, 855–70.
- Zhou Y, Ge WC and Wang QH** (2011) Petrogenesis of Mesozoic granite in Wulanhaote region, central Da Hinggan Mountains: constraints from geochemistry and Sr–Nd–Hf isotope. *Acta Petrologica et Mineralogica* **30**, 901–23 (in Chinese with English abstract).
- Zhou ZH, Lü LS, Yang YJ and Li T** (2010) Petrogenesis of the Early Cretaceous A-type granite in the Huanggang Sn–Fe deposit, Inner Mongolia: constraints from zircon U–Pb dating and geochemistry. *Acta Petrologica Sinica* **26**, 3521–37 (in Chinese with English abstract).
- Zhou ZH, Mao JW and Lyckberg P** (2012) Geochronology and isotopic geochemistry of the A-type granites from the Huanggang Sn–Fe deposit, southern Great Hinggan Range, NE China: implication for their origin and tectonic setting. *Journal of Asian Earth Sciences* **49**, 272–86.
- Zhu RX, Chen L, Wu FY and Liu JL** (2011) Timing, scale and mechanism of the destruction of the North China Craton. *Science China Earth Sciences* **54**, 789–97 (in Chinese with English abstract).
- Zhu RZ, Lai SC, Qin JF and Zhao SW** (2015) Early-Cretaceous highly fractionated I-type granites from the northern Tengchong block, western Yunnan, SW China: petrogenesis and tectonic implications. *Journal of Asian Earth Sciences* **100**, 145–63.
- Zhu XQ, Zhang Q, He YL, Zhu CH and Huang Y** (2006) Hydrothermal source rocks of the Meng'entaolegai Ag–Pb–Zn deposit in the granite batholith, Inner Mongolia, China: constrained by isotopic geochemistry. *Geochemical Journal* **40**, 265–75.